Available online at www.sciencedirect.com

ScienceDirect

Journal of Magnesium and Alloys 11 (2023) 2260–2284

www.elsevier.com/locate/jma

Review

Recent advances using equal-channel angular pressing to improve the properties of biodegradable Mg–Zn alloys

Mohammad Hashemi[a], Reza Alizadeh[a,*], Terence G. Langdon[b]

[a] *Department of Materials Science and Engineering, Sharif University of Technology, Tehran, Iran*
[b] *Materials Research Group, Department of Mechanical Engineering, University of Southampton, Southampton SO17 1BJ, United Kingdom*

Received 2 May 2023; received in revised form 8 July 2023; accepted 24 July 2023
Available online 7 August 2023

Abstract

Magnesium alloys are of considerable current interest for use as degradable implants due to their unique properties including biodegradability, biocompatibility, low density and adequate mechanical properties. Nevertheless, there is a need to further improve these properties either by alloying or through the use of appropriate processing. Among the different biodegradable Mg alloys now in use, the Mg–Zn series are of special interest and have been the subject of many research investigations. This is primarily because Zn is an essential element for the human body in addition to its positive effects in improving the mechanical strength and lowering the degradation rate of the implant. The properties of Mg–Zn alloys may be further improved both through the addition of third and fourth alloying elements such as Ca, Ag, Sn or Sr and/or by thermo-mechanical processing where the latter is more environmentally and economically favorable. In practice, procedures based on the application of severe plastic deformation (SPD) are especially suited to produce fine-grained microstructures with improved mechanical, degradation and cell behavior. Equal-channel angular pressing (ECAP) is a popular SPD technique that has the capability of producing bulk materials that are sufficiently large for use as typical implants. Accordingly, this review is designed to provide a comprehensive summary of the research that has been undertaken on ECAP-processed biodegradable Mg–Zn alloys.

Keywords: Bio-degradation; ECAP; Fine-grained microstructure; Mg–Zn alloys; Severe plastic deformation.

1. Introduction

Traditional metallic biomaterials, such as Co–Cr alloys, stainless steel, and titanium alloys, are frequently used as implants because of their superior physical and mechanical characteristics as well as their biological environmental adaptations [1]. The main drawbacks of these materials, however, are the high elastic modulus discrepancy between the implant and natural bone which produces a stress shielding effect and their inability to degrade in biological environments thereby requiring secondary surgery to remove the implant when the fractured bone tissue has healed sufficiently [2–4]. With the help of recent advances in material science that enabled the use of promising materials, the science of creating human implants that are biodegradable, nontoxic, and compatible with the intricate human body has advanced quickly in the field of medicine [5]. Magnesium alloys have attracted the most interest among the possible degradable implant materials and this has led to a demand for more research in this area [6–9]. Due to the similar density (1.74–2.0 g/cm^3) and tensile strength (100–200 MPa) to human bone, magnesium alloys are regarded as an essentially ideal candidate material for fracture therapies [10]. The similar elastic modulus of Mg alloys (41–45 GPa) to natural bone (10–30 GPa) would help to reduce the stress shielding effect and associated issues including implant loosening, skeleton thickening and major healing hindrances [11]. More importantly, magnesium, the fourth-most common cation in the human body, is crucial for human metabolism. Thus, an adult should consume between

* Corresponding author.
E-mail address: r.alizadeh@sharif.edu (R. Alizadeh).

https://doi.org/10.1016/j.jma.2023.07.009

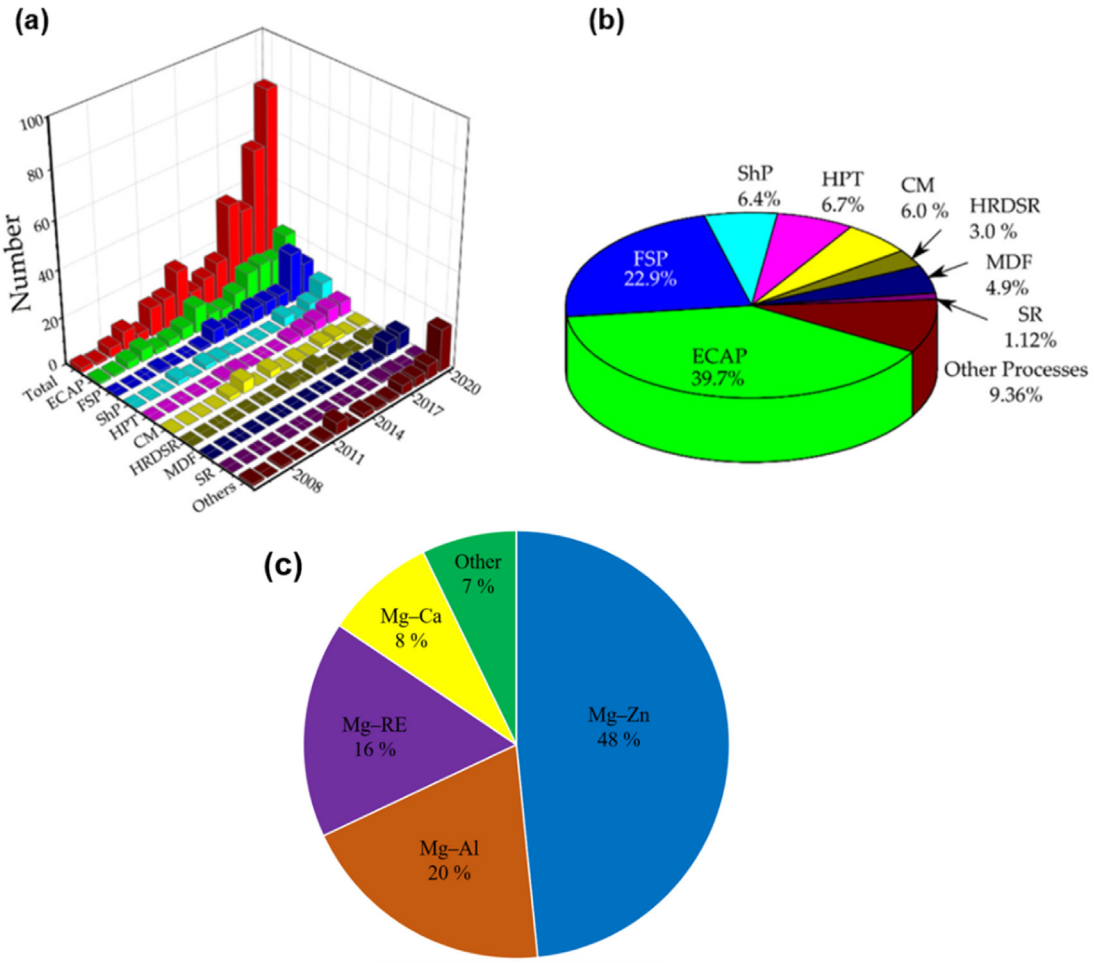

Fig. 1. (a) The number of research papers published by year from 2006 to 2020 for different SPD methods, and (b) a pie chart showing the contributions of different SPD methods to the published literature on the corrosion behavior of Mg alloys [46]. (c) Percentage of the number of articles published from 2019 to 2023 on different families of biodegradable magnesium alloys.

240 and 420 mg of magnesium daily, with any excess cations eliminated in the urine without causing any harm [12–14].

Magnesium and its alloys have a wide range of uses in the biomedical field although their use is constrained by their comparatively poor formability and corrosion resistance. The need to improve the formability and corrosion resistance of magnesium alloys for upcoming applications is therefore attracting considerable attention [15–17]. To address these difficulties, a number of strategies have been developed including alloying [18], heat treatment [10], coating [19,20] and the application of processing using severe plastic deformation (SPD) [21]. With reference to alloying and most of the coating processes, it should be noted that, although the advantages of these techniques are generally well established, special attention is needed to control the potential increase in cost and the environmental burden [22]. Accordingly, where possible it is necessary to improve the properties of biodegradable Mg alloys by secondary processes such as by heat treatment or by SPD without changing the chemical composition of the alloy, thereby negating the requirement of adding ternary or quaternary alloying elements.

In order to create fine-grained (FG, when the average grain size is in the range of 1–10 μm) or ultrafine-grained (UFG, when the average grain size is in the range of 100 nm−1 μm) or nano-grained (when the average grain size is smaller than 100 nm) biodegradable Mg alloys, a number of SPD techniques have been introduced and used to date, including equal-channel angular pressing (ECAP) [23–25], high-pressure torsion (HPT) [26,27], multidirectional forging (MDF) [28–30], cyclic extrusion and compression (CEC) [31–33], accumulative roll bonding (ARB) [34–36], severe shot peening (SSP) [37,38], rotary swaging (RSW) [39,40], and parallel tubular channel angular pressing (PTCAP) [41]. Among these various SPD techniques, it has been established that the use of ECAP shows the greatest efficiency in grain refinement for Mg alloys and this can greatly enhance the mechanical and electrochemical properties [7,42-45]. The importance of using ECAP is also evident from the large number of publications (Fig. 1a and b).

However, even when using SPD it is almost impossible to reach the desired properties of metallic implants when using pure magnesium. Fig. 1c depicts the distribution of articles

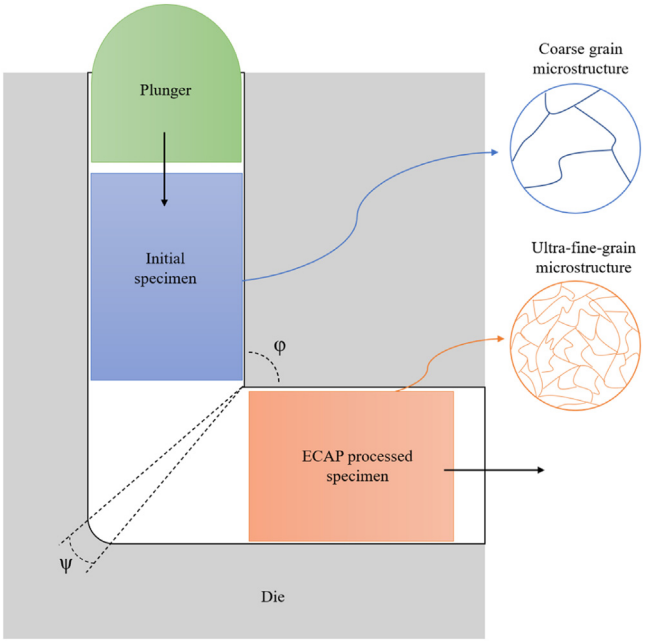

Fig. 2. Schematic representation of the ECAP process.

published from 2019 to 2023 across the various families of biodegradable magnesium alloys. It is readily apparent that nearly fifty percent of the publications are for Mg–Zn alloys where these alloys are of particular interest for biomedical applications [47]. The addition of a suitable amount of Zn can enhance the stability and quality of the corrosion film, as well as the charge transfer resistance and consequently the corrosion resistance of Mg, in addition to the effects of strengthening from both solution and precipitation hardening and grain refining [48,49]. Many studies have utilized the ECAP technique for improving the properties of biodegradable magnesium–zinc alloys as summarized in Table 1. Accordingly, and in order to provide a better understanding of the underlying mechanisms, challenges and more recent advances, this review is designed to summarize the effect of ECAP on the microstructure, mechanical properties, degradation behavior and biocompatibility of biodegradable Mg–Zn alloys.

2. Brief description of the ECAP process

According to the procedure developed for ECAP, the material is in the form of a rod or bar and it is pressed through a die constrained within a channel that maintains the same cross-sectional profile but is bent within the die through an internal channel angle of φ and with an angle of curvature of ψ, as shown in Fig. 2 [54]. There are also modifications to the ECAP method such as ECAP with an applied back pressure (ECAP-BP) [97] and double ECAP (D-ECAP) [59]. Each pass of deformation in ECAP generates a shear strain on the alloy. Eq. (1) illustrates how to determine the imposed equivalent strain (ε_{eq}) using the number of ECAP passes (N),

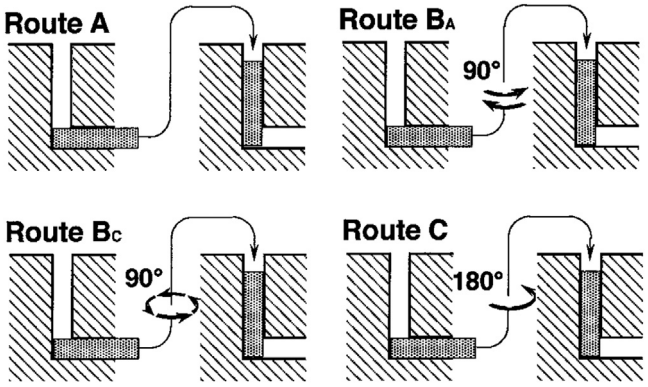

Fig. 3. Schematic representation of different ECAP routes [100].

die channel angle (φ), and corner curvature angle (ψ) [98].

$$\varepsilon_{eq} = N/\sqrt{3}\left[2\cot\left(\frac{\varphi+\psi}{2}\right)+\psi\,\mathrm{cosec}\left(\frac{\varphi+\psi}{2}\right)\right] \quad (1)$$

The final microstructure of Mg alloys can be greatly influenced by the ECAP processing route which is chosen based on the rotation arrangement between consecutive passes in addition to the degree of shear deformation [99]. Fig. 3 depicts a graphic representation of various routes.

From the experimental point of view, there exist several issues and challenges pertaining to the ECAP processing of magnesium alloys. Depending on the chemical composition of the alloy, and even the processing history of the material, ECAP processing conditions may be very different, as can be observed in Table 1, while an inappropriate choosing of these parameters would result in sample cracking and fracture. In this regard, and based on the unpublished work of the authors, while the extruded Mg–4Zn alloy can be successfully processed by ECAP at 200 °C, the extruded Mg–4Zn–0.5Ca alloy cannot be processed at this temperature. Therefore, it is imperative to optimize the processing parameters in such a way to prevent any damage to the sample during ECAP processing, taking into account the composition of the alloy and its mechanical properties.

3. Effect of ECAP on properties of biodegradable Mg–Zn based alloys

3.1. Physical properties

3.1.1. Microstructure evolution

The very large accumulated strains that are created during ECAP processing generally play an important role in the evolution of the microstructure and texture of magnesium alloys [68]. ECAP processing of Mg and Mg alloys is often carried out at relatively high temperatures, near to one-half of the melting point (0.5 T_m), because the hexagonal close-packed (HCP) crystal structure of magnesium only has two independent slip systems at low temperatures. As a result, dynamic recrystallization (DRX) is also crucial in microstructure and texture evolution of ECAP-processed Mg alloys. At the initial grain and twin boundaries, new very small grains are formed

Table 1
A summary of publications on ECAP-processed Mg–Zn based alloys indicating the nature of the ECAP conditions.

Alloy (%wt)	Φ (°)	Ψ (°)	T (°C)	Speed (mm/min)	Route	Number of passes	Ref.
Mg–3Zn–0.6Zr (ZK30)	90	20	250	10	Bc	1, 2, 4	[5]
Mg–4 Zn	90	20	220	–	Bc	4	[20]
Mg–4Zn–0.5Ca							
Mg–1.84Zn–0.52Nd (ZN20)	–	–	300, 350	30	Bc	4	[50]
Mg–1.84Zn–0.52Nd (ZN20)	–	–	300	30	Bc	4	[51]
Mg–3Zn–0.6 Zr (ZK30)	90, 120	20	250	10	A, Bc, C	1, 2, 4	[52]
Mg–1.0Zn–0.2Ca	120	–	350, 400, 430	–	Bc	1, 2	[53]
Mg–3Zn–0.6Zr–0.4Mn	90	20	250	10	Bc, A, C	1, 4	[54]
Mg–3Zn–0.6Zr–0.4Mn	120	20	250	10	Bc	1, 2, 4	[55]
Mg–6.12Zn–0.65Zr (ZK60)	120	25	240	60	Bc	6	[56]
Mg–4.18Zn–1.08Mn	110	–	300	60	Bc	1–4	[57]
Mg–1.8Zn–0.7Mn–0.02Fe–0.02Ni (ZM21)	110	30	220	–	Bc	4	[58]
Mg–0.6Zn–0.5Ca (ZX00)	90+90	–	350–220	120	Bc	1, 2, 4	[59]
Mg–1.62Zn–0.55Zr-0.38Y	90	20	380	–	Bc	2, 4	[60]
Mg–4.71Zn–0.6Ca	90	20	250	60	Bc	4	[61]
Mg–4.08Zn–1.53Si	110	–	300	60	Bc	1–4	[62]
Mg–2Zn–xGd–0.5Zr (x = 0, 0.5, 1, 2)	90	20	380	–	Bc	1, 2, 4	[63]
Mg–3.9Zn–1.1RE–0.56Zr (ZE41)	110	30	300, 275	–	Bc	1–6	[64]
Mg–1Zn–0.2Ca	120	–	400	6	Bc	1, 2, 4	[65]
Mg–1.0Zn–0.3Ca	120	–	400, 300	–	Bc	10	[66]
Mg–1.8Zn–0.7Si–0.4Ca	120	0	350–400	10.2	Bc	1–4	[67]
Mg–5.0Zn–0.5Ca–0.3Mn	90	37	250	–	Bc	1–4	[68]
Mg–6Zn	90	–	320	90	Bc	2, 6	[69]
Mg–6Zn	90	–	200	90	Bc	6	[70]
Mg–6.52Zn–0.95Y	90	37	200, 300	–	Bc	1, 2, 4	[71]
Mg–2Zn–0.5Mn–1.2Ca–1.35Ce	90	–	300	30	–	12	[72]
Mg–1Zn–0.2Ca	120	–	250, 300, 350, 400	6	–	2, 4, 6, 8	[73]
Mg–6 Zn	90	0	220, 160	–	Bc	1–4	[44]
Mg–12Zn			200, 185, 170, 155				
Mg–6Zn–0.6Zr–0.4Ag–0.2Ca	90	0	200, 150, 125	4.5, 2.25	A, C	1, 2, 4	[74]
Mg–6Zn–0.5Zr	120	–	250, 320	–	Bc	2	[75]
Mg–6.08Zn–0.56Zr (ZK60)	90	–	300–150	–	–	8, 12	[76]
Mg–5.46Zn–0.55Zr (ZK60)	90	37	250	–	Bc	1–4	[77]
Mg–2Zn–0.98Mn (ZM21)	–	–	250	20	Bc	8	[78]
Mg–6Zn–0.3Zr (ZK60)	90	20	180, 200, 220	120	–	4	[79]
Mg–1.7Zn–0.8Mn (ZM21)	110	20	200, 150	30	Bc	4	[80]
Mg–6Zn–0.5Zr (ZK60)	90	20	220	60	Bc	1, 2, 4, 8	[81]
Mg–5.49Zn–0.55Zr (ZK60)	90	37	250	–	Bc	1–4	[82]
Mg–5.3Zn–0.48Zr (ZK60)	110	20	250, 200, 150	30	Bc	1–8	[83] [84]
Mg–5.6Zn–0.6Zr (ZK60)	90	20	240, 180	20	Bc	4, 8	[85]
Mg–5.5Zn–0.5Zr (ZK60)	90, 110, 135	20	200	420	–	1	[86]
Mg–4Zn–0.7Zr–1.4(Ce + La) (ZE41)	90	–	320	4	rotated by 120°	1–6	[87]
Mg–5.5Zn–0.5Zr	90	20	200	420	Bc	1, 2, 4, 6, 8	[88]
Mg–5.25Zn–0.6Ca	90	37	250	–	A, Bc, C	4	[89]
Mg–5.12Zn–0.32Ca	90	37	250	600	Bc	4	[90]
Mg–5.5Zn–0.5Zr (ZK60)	90	20	200	–	Bc	8	[91]
Mg–4.9Zn–1.4RE– 0.7Zr (ZE41A)	–	–	330	–	–	8–32	[92]
Mg–4.9Zn–1.4RE–0.7Zr (ZE41A)	–	–	330	–	A	8, 16, 32, 60	[93]
Mg–3Zn–0.2Ca	120	0	320	120	A	2, 4, 6, 8	[94]
Mg–6Zn–0.5Zr (ZK60)	120	–	350	–	C	2	[95]
Mg–1Zn–0.3Ca	120	–	300–400	–	Bc	10	[96]

as a result of DRX with specific crystallographic orientations [59]. Fig. 4 schematically shows the microstructure evolution caused by ECAP. Typically, the as-cast alloy has a microstructure with coarse grains at the initial step (Fig. 4a). Large numbers of dislocations move within the grains towards the grain boundaries during ECAP (Fig. 4b) and they are subsequently blocked by the initial grain boundaries thereby creating a complex network of dislocation entanglements (Fig. 4c) [56]. Entangled dislocations can easily rearrange, evolve into dislocation walls, and eventually change into substructures

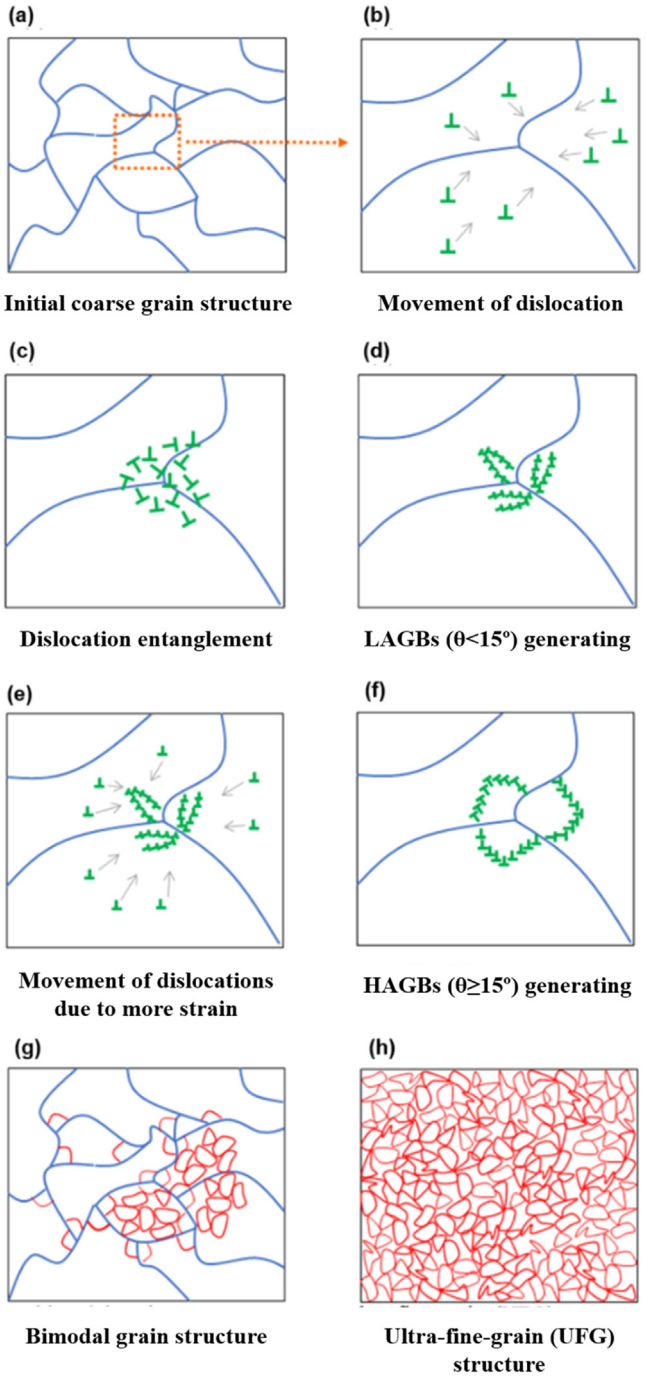

Fig. 4. Microstructure evolution of magnesium alloys during ECAP processing.

making low energy dislocation structures (LEDS) [101]. As the strain increases, sub-grain boundaries absorb dislocations to generate low-angle grain boundaries (LAGBs) (Fig. 4d) which can continue to absorb dislocations (Fig. 4e) and eventually transform into high-angle grain boundaries (HAGBs) (Fig. 4f) [102].

The overall dislocation density, ρ_t, is directly correlated with the average sub-grain size (d) by means of [103]

$$d = \frac{K}{\sqrt{\rho_t}} \tag{2}$$

where K is a constant which is dependent on the total dislocation density. Dislocations during the ECAP processing can be divided into two main categories with different properties: dislocations forming the cell structure and those placed within the cells. Thus, the overall dislocation density can be defined as [85]

$$\rho_t = f\rho_w + (1-f)\rho_c \tag{3}$$

where f denotes the volume fraction of the cell walls and ρ_w and ρ_c are the density of dislocations placed on the wall and cell interior, respectively.

A bimodal grain structure (Fig. 4g) is reported to be produced during the initial passes of ECAP as a result of inhomogeneity of slip and deformation in deferent grains. Slip does not occur in all grains in the same way and it is possible that the slip systems become active only in some grains. As a result, grains with more suitable orientations are deformed and refined earlier, leaving less deformed and coarser grains that eventually will be deformed later [82]. Incomplete DRX was recognized as a contributing factor in the creation of the bimodal grain structure and the following attributes are introduced as the key causes [68]: (i) the total equivalent strain generated by the first ECAP pass does not have sufficient energy for a successful complete recrystallization, (ii) random texture favors only some grains to accommodate the imposed strain, and (iii) the coarse secondary phase particles are harder when compared to the Mg matrix and they tend to collect local strains giving the particle stimulated nucleation or PSN effect and this in turn accelerates the recrystallization process surrounding them [104]. With repeated ECAP passes, the unrecrystallized coarse grains would be converted to find DRX grains and the entire structure would be uniformly and homogeneously altered into a UFG structure (Fig. 4h). This development has been reported for ZK30 alloys [5]. Processing in a single pass (1-P) revealed a heterogeneous structure with large elongated grains and a bimodal grain size distribution, as well as an increase in LAGB (white and red lines) density of 225% compared to the as-annealed (AA) counterpart (Fig. 5a-d). It can be observed that an FG microstructure (the average grain size is about 1.94 μm) is obtained after four ECAP passes (Fig. 5e and f) which resulted in decreasing the LAGBs by 25.4% and increasing 4.4% in the HAGBs compared to the 1-P counterpart since LAGBs are transferred into HAGBs.

The processing route, die angle and temperature, in addition to the numbers of passes, affect the grain size distribution obtained after ECAP. According to an earlier report [89], route A was the least successful technique for refining grains, followed by route C, which was more efficient than route A, while route Bc, was the most effective. It was also reported [52] that a die angle of $\varphi = 120°$ produces coarser grains compared to a die angle of $\varphi = 90°$ because the latter underwent greater strain.

Regarding the effect of numbers of passes, it was reported [56] that when ZK60 alloy with an average grain size of 102 μm is subjected to ECAP processing, the grain size is reduced to 7.4 μm after 4 passes and 3.5 μm after 6 passes.

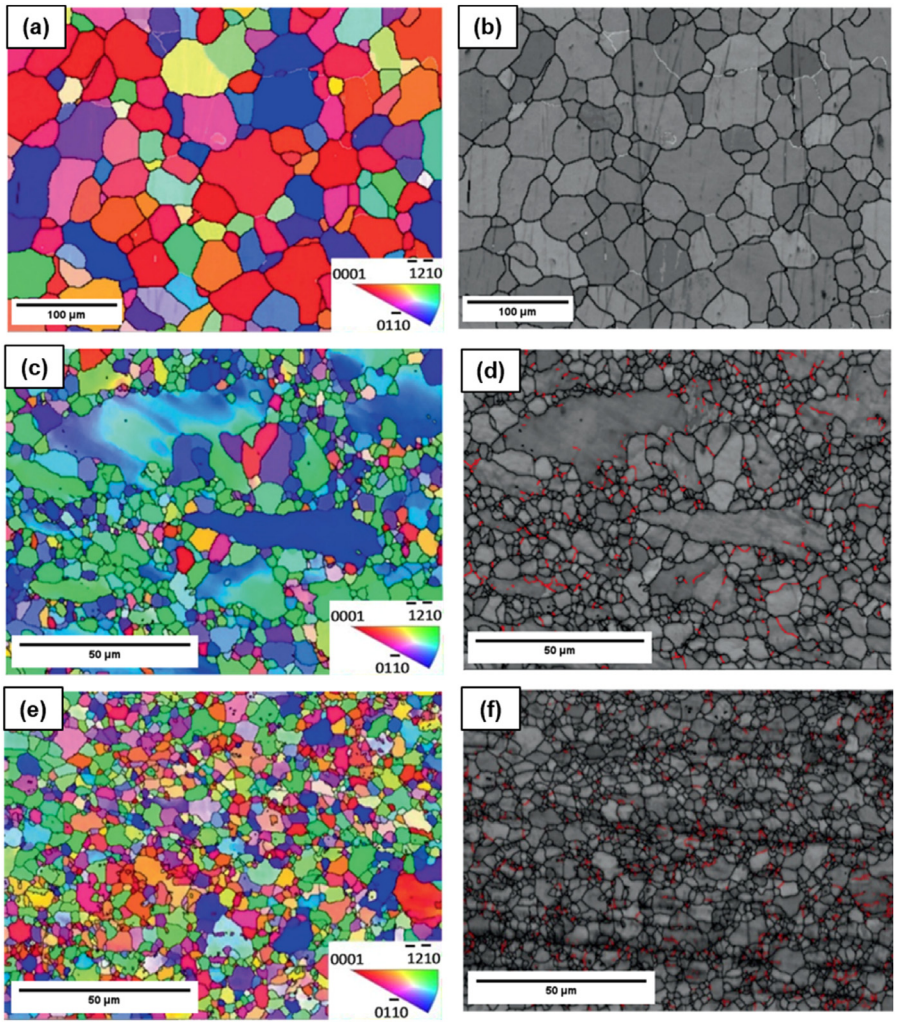

Fig. 5. Inverse pole figure maps (a,c,e) and their corresponding grain boundary maps (b,d,f) for the AA ZK30 (a,b) and the ECAP processed samples for different numbers of passes: (c,d) 1-P, (e,f) 4-Bc. Reproduced from [5].

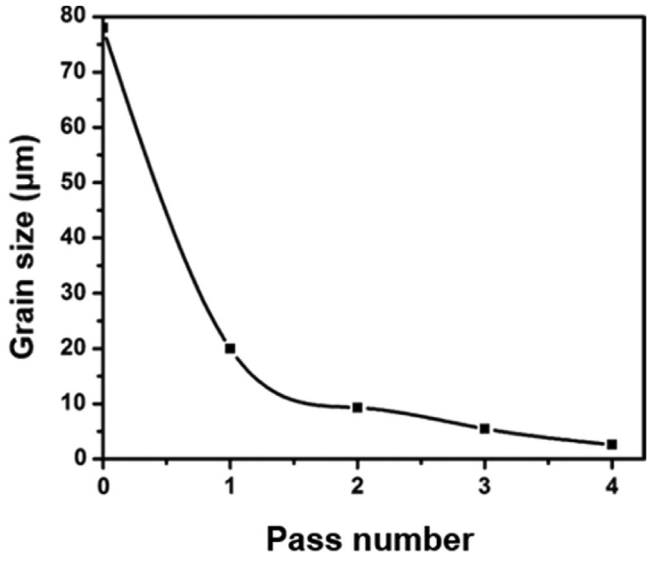

Fig. 6. Variation of grain size of an Mg–1.8Zn–0.7Si–0.4Ca alloy with number of ECAP passes. ECAP processing temperature was 350 °C [67].

Fig. 6 exhibits the grain size of an Mg–1.8Zn–0.7Si–0.4Ca alloy processed by ECAP at 350 °C versus the pass number. In accordance with this plot, the grain size of the specimen is reduced from 78 μm in the solution state (not processed by ECAP) to about 20, 9.5, 5 and 3 μm as the number of ECAP passes increases through 1, 2, 3 and 4, respectively. The first pass experiences the greatest grain size reduction, and therefore a greatest grain refinement efficiency, and as the number of passes is increased, the grain size changes become less significant [67].

The processing of D-ECAP involves two angled channels in one mold so that each pass equals two conventional passes. Fig. 7 summarizes the grain sizes and values of the area fractions of large grains of several tens of microns obtained following D-ECAP processing of a ZX00 alloy at different temperatures and different numbers of passes. As can be seen, the area fraction of large grains drops with an increase in the number of passes while the grain size is reduced with a decrease in the D-ECAP temperature [59].

The effect of ECAP on precipitation is shown in Fig. 8 where XRD patterns of the ZK30 alloy in the solution state

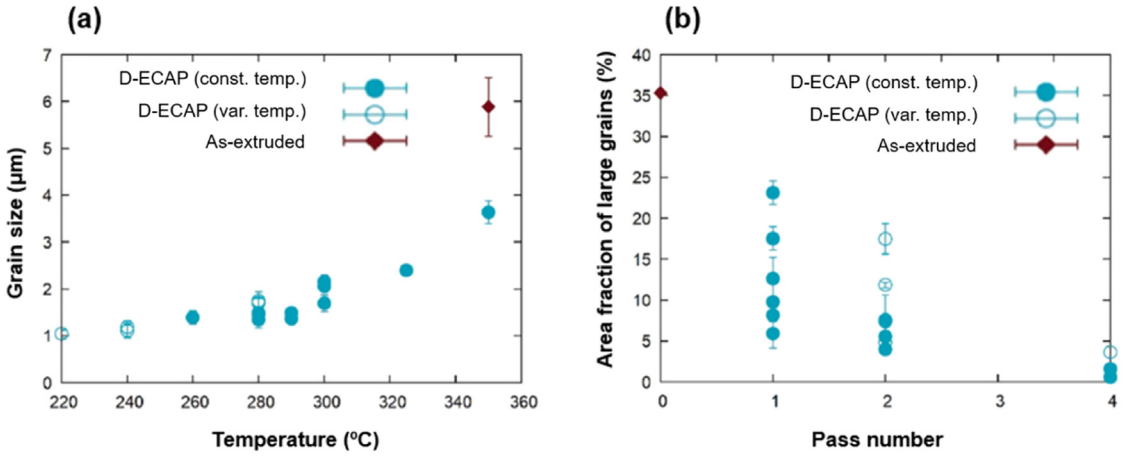

Fig. 7. (a) Grain size as a function of the temperature of the D-ECAP process (minimum temperature applied). (b) Area fraction of large grains as a function of the number of D-ECAP passes. Full symbols indicate samples where the D-ECAP process was conducted at constant temperature, while open symbols represent results obtained on samples where the processing temperature was varied between the passes [59].

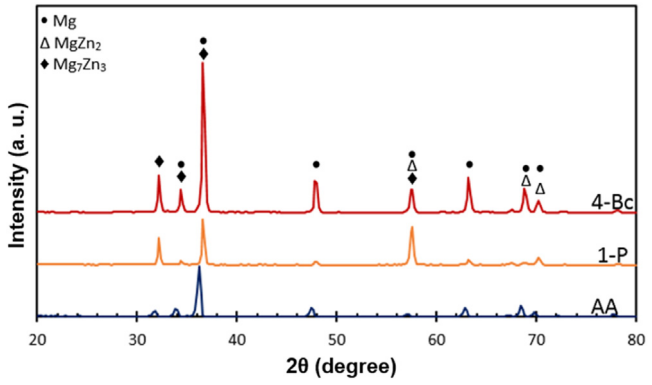

Fig. 8. XRD patterns of the ZK30 alloy before (AA) and after ECAP processing through 1 pass (1-P) and 4 passes via route Bc (4-Bc) [55].

(AA) are compared with those after ECAP processing through 1-P and 4-P which respectively represent samples processed by 1 and 4 passes. It is apparent that the AA condition was almost entirely a single phase α-Mg solid solution. Notably, the production of precipitates was induced by performing ECAP on the samples. By increasing the number of passes up to 4, the peaks corresponding to the second phases increase in number and intensity [55] where this increase is a result of recrystallization during ECAP [105].

In addition to precipitate formation, other changes such as particle breaking or even particle dissolution in the matrix may also occur during ECAP. For example, it was reported that [63] after ECAP the network structure of the second phases in Mg–2Zn–xGd–0.5Zr (where x = 0, 0.5, 1, 2) alloys was shattered to a granular morphology. Fig. 9 from another investigation [60] shows the transmission electron microscopy (TEM) images of the extruded and four pass extruded Mg–1.62Zn–0.55Zr–0.38Y alloy. The major large second phase for the extruded alloy prior to ECAP extrusion was the W phase ($Mg_3Y_2Zn_3$) (Fig. 9a). Also, the second dispersive phases were spread in the form of a short rod-like format (Fig. 9b). A breakage of the $Mg_3Y_2Zn_3$ particles was observed after ECAP processing for four passes (Fig. 9c) as the result of particle cutting by dislocations. This led to a great improvement in uniformity of the distribution of second phase particles (Fig. 9d).

An ECAP-stimulated solution treatment was studied in the Mg–6Zn alloy [69], and the corresponding scanning electron microscopy (SEM) images are presented in Fig. 10. As can be observed in Fig. 10, by performing ECAP at 320 °C the amount of intermetallic phase is reduced both in number and size with increasing numbers of passes and these particles are almost completely dissolved after 6 passes (Fig. 10a-c). By contrast, solution-treated alloys had a significant amount of remaining intermetallic particles even after a 24-hour heat-treatment as illustrated in Fig. 10d-f. Accordingly, it is clear that at the same temperature the ECAP-stimulated solution treatment outperformed the traditional isothermal solution treatment with respect to the ability to prepare a single-phase Mg–6Zn alloy [69]. Accordingly, it can be concluded that depending on the material and also processing parameters such as temperature processing by ECAP may have different effects on second-phase particles [59].

3.1.2. Texture evolution

Another important effect of ECAP on the Mg alloys, in addition to the microstructural changes, is texture modification. The composition of the alloy, the initial grain size and ECAP-related characteristics, including temperature, processing route and numbers of passes, all affect the evolution of texture in magnesium alloys processed by ECAP [86]. It is commonly assumed that cast magnesium alloys have a random texture but extruded magnesium alloys have a fiber texture [80,84]. However, following ECAP the original texture of cast and wrought magnesium alloys tends to disintegrate, eventually weakening and causing the creation of new texture elements [80,84,106,107]. Fig. 11 shows the basal pole figures of the ZM21 Mg alloy in the rolled and ECAP-processed conditions. According to Fig. 11a, the rolled alloy displayed

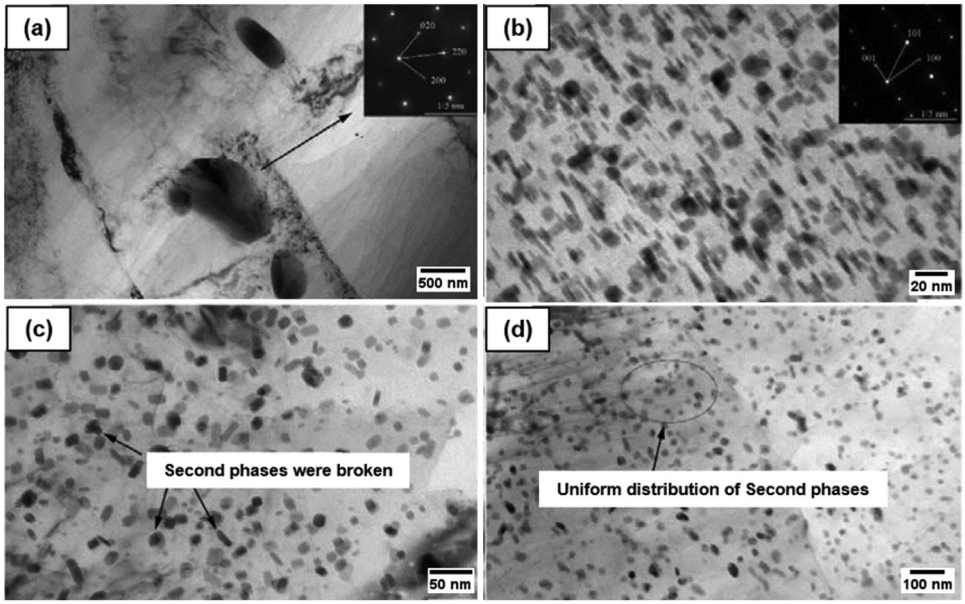

Fig. 9. TEM images of the Mg–1.62Zn–0.55Zr–0.38Y alloy in the extruded (a,b) and ECAP processed for four passes (c,d). Reproduced from [60].

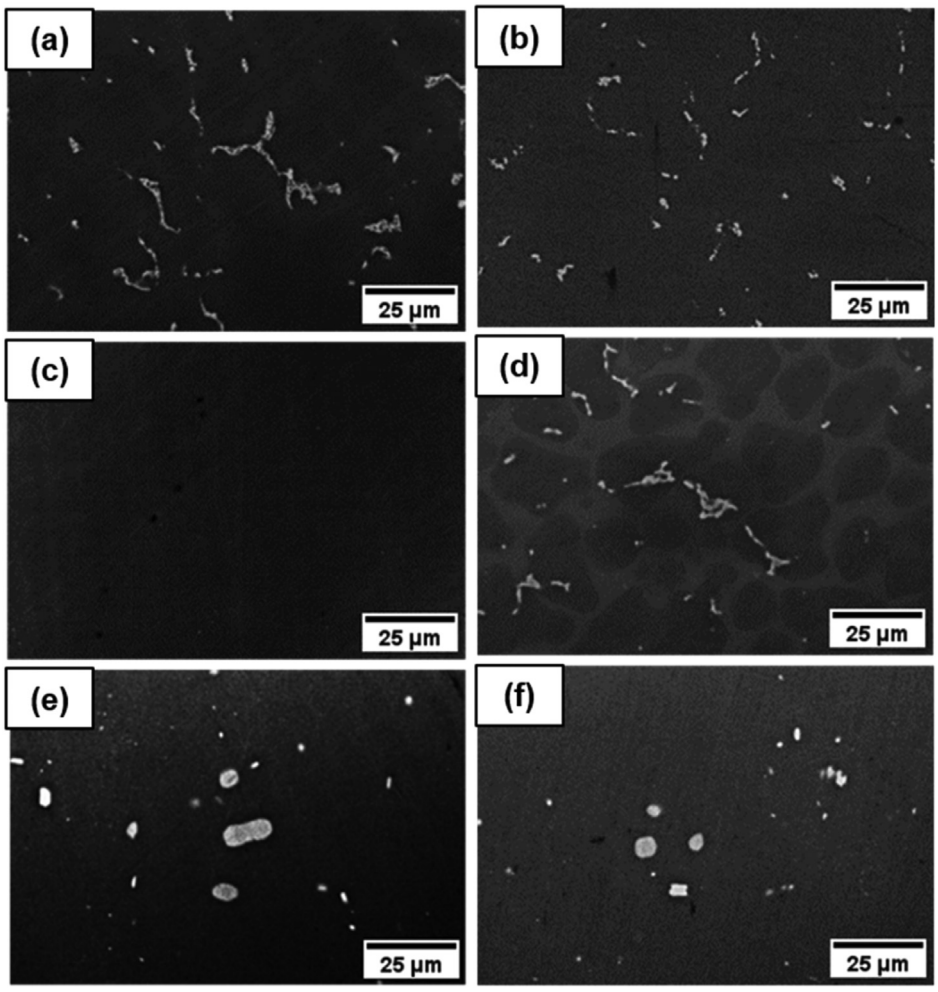

Fig. 10. SEM micrographs of Mg–6 Zn alloys. (a) Non-processed; ECAP-stimulated solution treated for (b) 2 passes and (c) 6 passes; solution treated for (d) 8 h, (e) 16 h and (f) 24 h. Reproduced from [69].

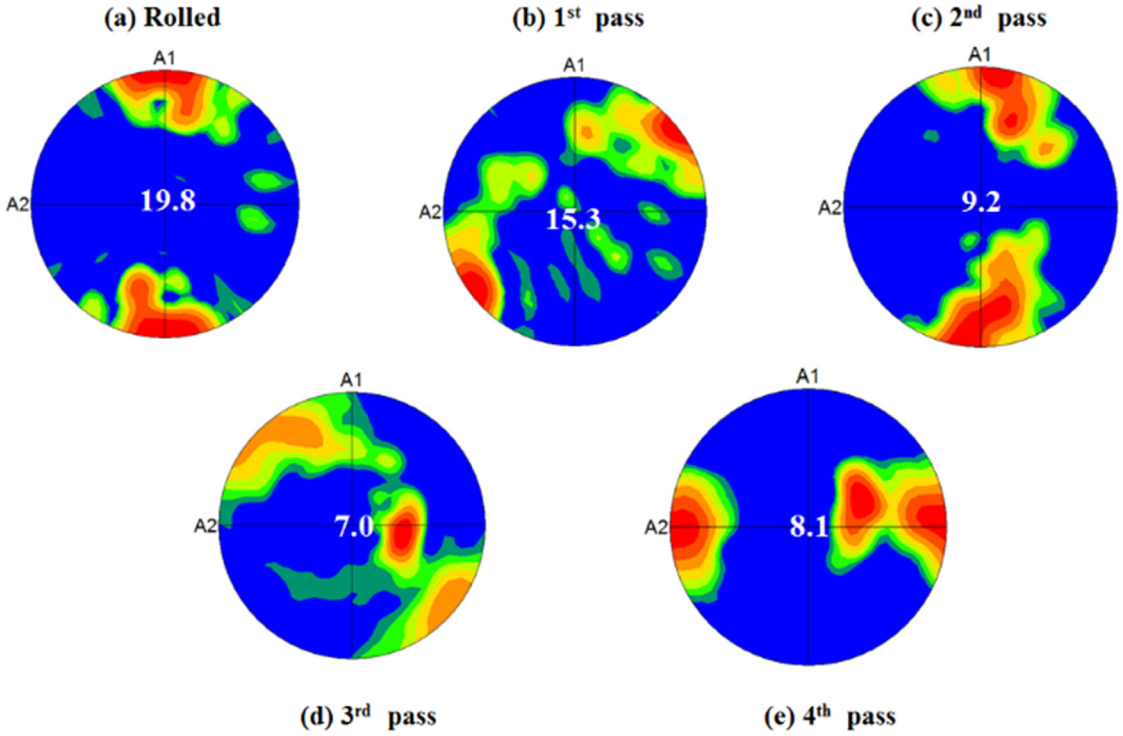

Fig. 11. Basal pole figures of the ZM21 alloy. (a) Rolled, (b) 1st pass, (c) 2nd pass, (d) 3rd pass and (e) 4th pass ECAP. A1: Extrusion direction or RD, and A2: Transverse direction or TD [58].

a texture with a maximum intensity of 19.8 MRD (multiples of random distribution) along the rolling direction (RD). After the first ECAP pass (Fig. 11b), the texture element shifted by 45° to the RD/TD (transverse direction), and the texture intensity also decreased to some extent. The rotation of the ZM21 Mg sample by 90° counterclockwise between each pass of the ECAP is connected to the change in the location of the highest texture intensity. While the texture intensity on the second pass of the ECAP was reduced to a value of 9.2 (Fig. 11c), the texture along the RD was equivalent to the rolled ZM21 alloy. However, the texture moved away from RD and TD as a result of the fourth pass of ECAP. The relative drop in texture intensity from 19.8 in the rolled condition to 15.3, 9.2, and 7.0 following the first, second, and third passes of the ECAP, respectively, is also an intriguing characteristic. By contrast, by the end of the fourth pass there was a marginal rise in pole intensity of 8.2 (Fig. 11e). Furthermore, the texture of the ZM21 alloy after the fourth pass was parallel to RD. The original texture element is weakening as evidenced by the decrease in texture intensity from the rolled condition to the third ECAP pass (Fig. 11a-d). The emergence of a new texture element is indicated by the minor rise in texture intensity [58].

Undoubtedly, an experimental measurement of texture is crucial, but predicting texture by simulation would be also of great importance and interest. In fact, accurate texture prediction is necessary for comprehending and forecasting the anisotropic mechanical behavior. Also, it can aid in designing for superior regulation and energy efficiency during the forming processes. Generally, texture modeling is widely recognized as a critical tool for texture control [108]. In this regard, texture evolution during the ECAP treatment of a ZK60 alloy has been modeled using visco-plastic self-consistent (VPSC) simulations [86]. The experimental findings presented in Fig. 12 indicate that the original texture undergoes only minor alterations following a single pass through the die with an angle of 110°, and essentially no changes were observed using a die with an angle of 135°. These observations align with the predictions made by the simulations presented in Fig. 13, which forecast a gradual development of texture. It is noteworthy that even after four passes, no significant change in the original texture was observed using the 135° die angle. Furthermore, the amount of strain applied per pass in the dies with channel angles of 90°, 110°, and 135° is approximately 1.1, 0.8, and 0.5, respectively [98]. As such, it can be concluded that an increase in the die angle leads to a slower development of texture [86].

3.1.3. Deformation modes

Due to their low critical resolved shear stress (CRSS), basal slip and twinning are the main deformation modes for magnesium alloys at room temperature [50]. It is well known that the basal slip system, $(0001)<11\bar{2}0>$, has a significantly lower CRSS than non-basal systems, making it the dominant slip system for magnesium at room temperature [109]. In the early stages of plastic deformation, twinning can cause an abrupt drop in stress within a grain and this may cause twinning in nearby grains [110] and promote slip deformation in

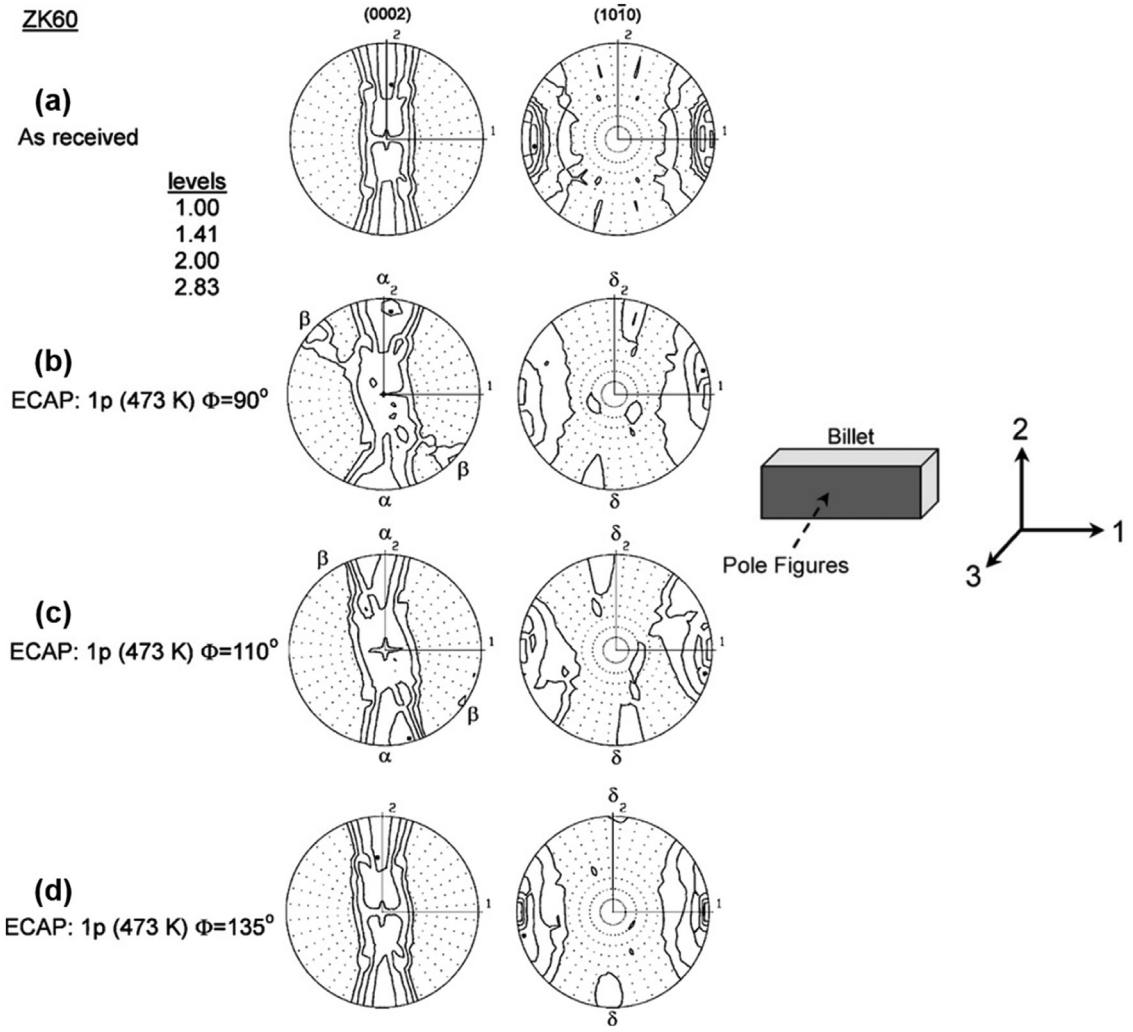

Fig. 12. Experimental (0002) and (10$\bar{1}$0) pole figures, determined on the flow plane of the ZK60 billets in the as-received (a) and ECAP processed conditions, using dies with channel angles of 90° (b), 110° (c) and 135° (d). Reproduced from [86].

initially unfavorably orientated grains as a result of crystal rotation accompanied by twinning [6]. The relationship between the *c*-axis and the loading direction has a significant impact on the type of twinning occurring during the deformation [50,111]. When the sample is stretched along the *c*-axis tension twins ($\{10\bar{1}2\}<10\bar{1}\bar{1}>$) are generated, but when the sample is compressed along the *c*-axis only contraction twins ($\{10\bar{1}1\}<10\bar{1}\bar{2}>$) are generated. Additionally, since the CRSS of tension twins (2 MPa [112]) is substantially lower than for contraction twins (114 MPa [113]), tension twins are more likely to appear [50,87].

By increasing strain during ECAP as a result of crystal rotation during twinning, and since basal slip does not meet the von Mises condition of at least five independent slip systems, the cross-slip of *a*-dislocations from the basal planes to the prismatic planes can take place [91]. This is evident from the data presented in Table 2 for an ECAP-processed Mg–1Zn–0.3Ca alloy. When the orientation factor is less in a slip system, it becomes comparatively more active than other slip systems. The basal slip systems were the most active in the initial condition whereas the prismatic slip systems were less active. The high ECAP-induced texture encouraged the activation of prismatic slip, which replaced the basal slip systems as the major deformation mode since the corresponding orientation factor dropped rapidly. The activity of the twinning and pyramidal slip system did not vary significantly [66].

Accordingly, depending on the alloy and ECAP processing parameters (Table 1), some important microstructural changes, such as grain refinement, secondary phase morphology modification and texture modification, may happen in the microstructure, where these changes can affect the mechanical, corrosion, and biological properties of these magnesium alloys. In the sections that follow, these consequences are comprehensively reviewed.

3.2. Mechanical properties

3.2.1. Strengthening mechanisms

Mechanical properties are influenced by the microstructural changes that are produced during ECAP processing as

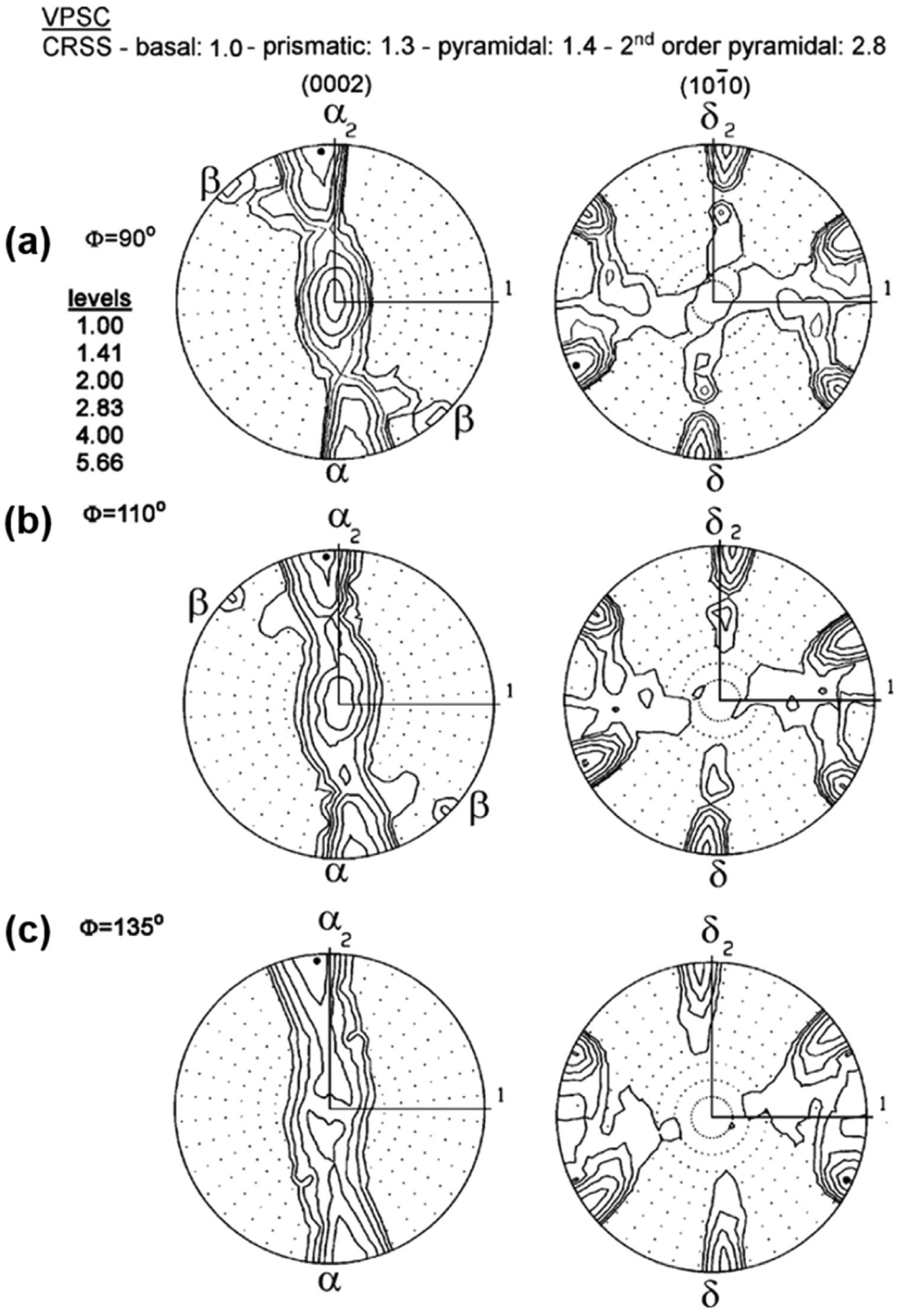

Fig. 13. Predicted (0002) and (10$\bar{1}$0) pole figures of the ECAP processed ZK60 alloy, determined by the VPSC simulations, for different die channel angles of 90° (a), 110° (b), and 135° (c) [86].

Table 2
Orientation factors for the Mg–1Zn–0.3Ca alloy in the initial state and after ECAP processing [66].

Processing	Basal slip (0001)<11$\bar{2}$0>	Prismatic slip {10$\bar{1}$0}<11$\bar{2}$0>	Pyramidal slip <c + a>	Twinning {10$\bar{1}$2}<10$\bar{1}$1>
Initial state	4.4	5.1	4.7	4.8
ECAP	5.9	3.9	4.9	4.8

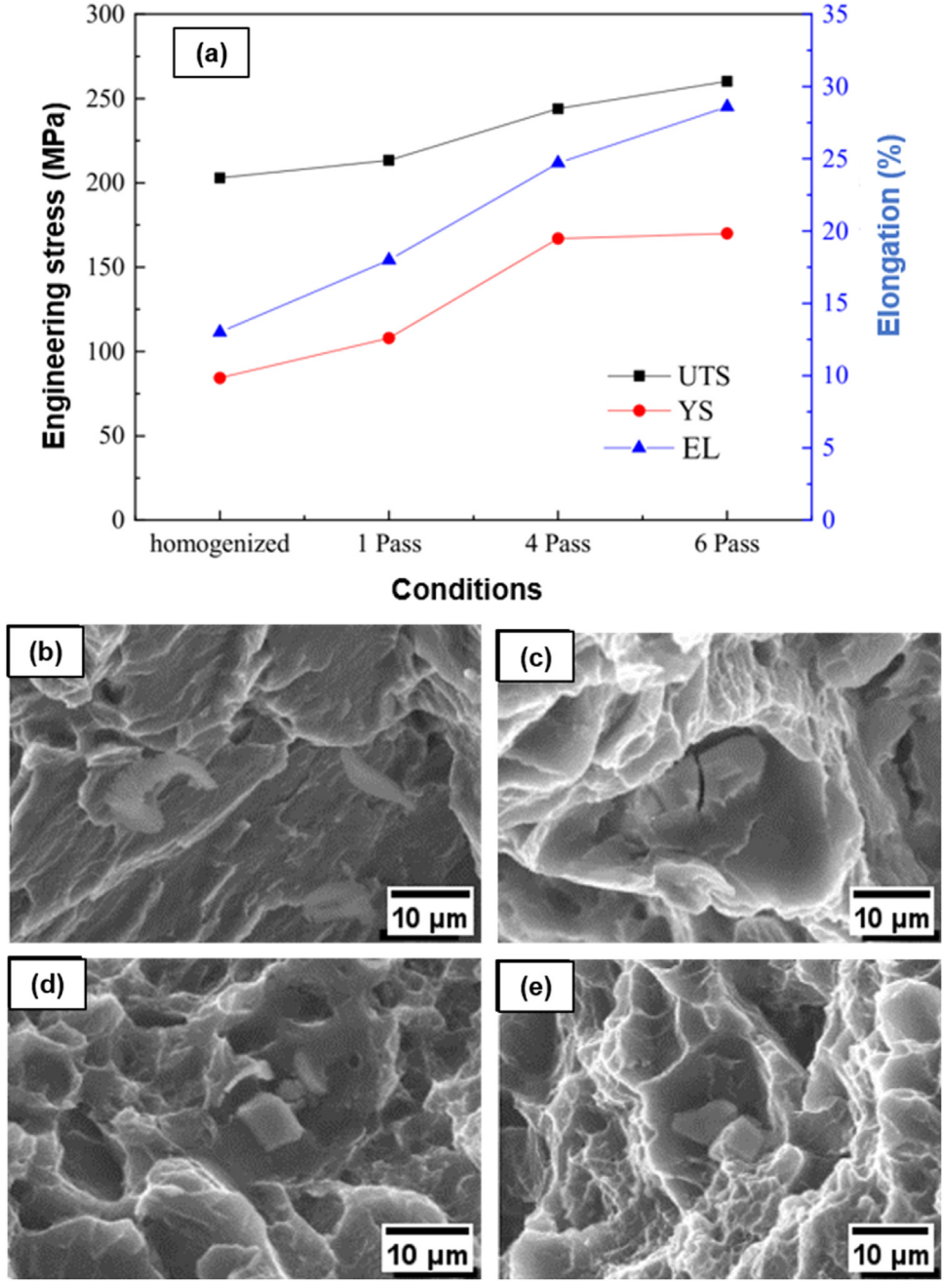

Fig. 14. (a) Summary of the mechanical properties obtained from tensile tests on the ZK60 alloy in the homogenized and ECAP-processed conditions [56]; Tensile fracture surfaces of the ZK60 alloy in the homogenized (b) and ECAP processed conditions (c-e), where the number of ECAP passes is 1 (c), 4 (d) and 6 (e). Reproduced from [56].

discussed in the previous section. Generally, the grain size, texture and morphology of the precipitates have a significant impact on the mechanical characteristics of magnesium alloys at room temperature [68]. Three primary strengthening mechanisms in extruded and ECAP-processed Mg alloys are grain boundary strengthening, precipitate strengthening and solid solution strengthening [50]. The polycrystalline material yield strength (or hardness) follows the established Hall-Petch relationship [114]:

$$\sigma_y = \sigma_0 + kd^{-\frac{1}{2}} \quad (4)$$

where σ_y is the yield strength, d is the grain size, σ_0 and k are experimentally derived constants, which are known as the overall resistance of the lattice to dislocation movement and the locking parameter of the grain boundaries, respectively. For Mg systems, the k values of 0.13 MPa $m^{1/2}$ for fine grains (17–30 μm) and 0.7 MPa $m^{1/2}$ for coarse grains (30–87 μm) have been reported [115] while σ_0 in coarse grains is lower than in fine grains [50]. A recent analysis showed that pure Mg and Mg alloys exhibit Hall-Petch behavior which is consistent with many other metals having different crystal structures [116].

It should be mentioned that the sample texture may have an impact on the k value. The sample would display a high grain size strengthening effect, for example, when most of the textured planes are orientated for hard slip with a high Hall Petch constant [87]. According to a recent report [50], the yield strength of samples made from ZN20 alloy can be described as follows:

$$\sigma_y = \sigma_{gs} + \sigma_{ps} + \sigma_{ss} \tag{5}$$

where σ_{gs}, σ_{ps}, and σ_{ss} are the grain boundary strengthening, precipitates strengthening and solid solution strengthening, respectively. In bimodal grained samples, the contribution of grain boundary strengthening to the strength, σ_{gs}, can be expressed as follows [50]:

$$\sigma_{gs} = \left(\sigma_f + k_f d_f^{-\frac{1}{2}}\right) f_f + \left(\sigma_c + k_c d_c^{-\frac{1}{2}}\right) f_f \tag{6}$$

where σ_f, k_f and d_f are the friction stress, constant and grain size of fine grains, σ_c, k_c and d_c are the friction stress, constant and grain size of coarse grains, and f_f and f_c are the volume fractions of fine grains and coarse grains, respectively.

Because the second phase may prevent dislocations from moving, the strength of precipitate-containing magnesium alloys can be effectively increased. The Orowan strengthening mechanism serves as an example of the manner by which the second phase affects the prevention of dislocation motion. However, it has been demonstrated [63] that during severe plastic deformation strengthening by grain refinement was superior to second phase strengthening. The effect of precipitate strengthening (σ_{ps}) on strength can therefore be expressed as follows [50]:

$$\sigma_{ps} = M \frac{Gb}{2\pi\sqrt{1-\upsilon}\left(\frac{0.953}{\sqrt{f}} - 1\right)d_p} \ln\frac{d_p}{b} \tag{7}$$

where M is Taylor factor with a range of 2.1–2.5, G is the shear modulus (16.6 GPa at room temperature), b is the Burgers vector (3.2×10^{-10} m), υ is Poisson's ratio (0.35) and d_p and f are the average size and volume fraction of the second phase, respectively.

The impact of solid solution strengthening (σ_{ss}) on strength can then be modeled as follows [50]:

$$\sigma_{ss} = \left(k_{Zn}^{\frac{1}{n}} C_{Zn} + k_{Nd}^{\frac{1}{n}} C_{Nd}\right) \tag{8}$$

where k and C represent the solution strengthening constant and atom fraction and n is a constant which is usually treated as 1/3 or 2/3.

3.2.2. Mechanical behavior

Fig. 14a summarizes the effect of ECAP on the tensile mechanical properties of the ZK60 alloy. These findings reveal that as the number of ECAP passes rises so both the strength and ductility improve. The fracture elongation of the alloy is improved from 8.0% in the homogenized state to 24.7% after processing by four ECAP passes, thereby demonstrating a significant improvement in ductility at room temperature. Also, the synergistic effect of grain refinement and second phase strengthening was introduced as responsible for the high values obtained for the UTS, YS and elongation of the alloy after

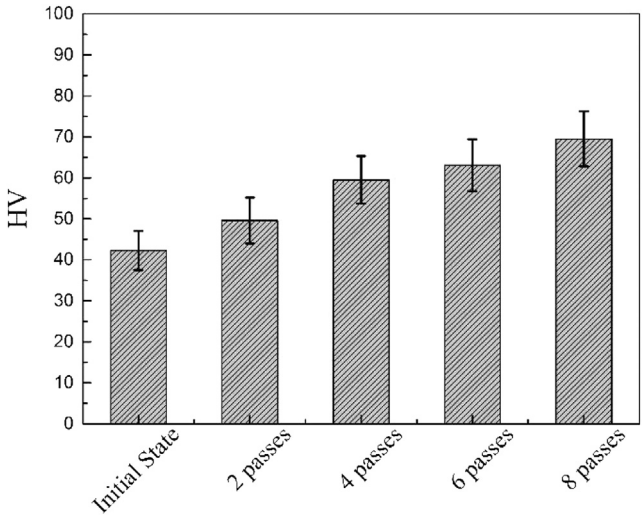

Fig. 15. Effect of ECAP on the microhardness values of the Mg–1Zn–0.2Ca alloy [73].

6 ECAP passes which are 258 MPa, 170 MPa and 28.60%, respectively [56]. Other research [63,73] also gave similar findings for other Mg–Zn based alloys. An explanation for the observed improvement of ductility in ECAP-processed alloys can be the increase in the fraction of HAGBs [82,90] which can affect both the deformation and fracture modes. Fig. 14b-e displays SEM fracture surfaces of the ZK60 tensile specimens where a summary of the tensile test results is shown in Fig. 14a. According to Fig. 14b, the fracture surface of the homogenized alloy exhibits a considerable region of cleavage planes, demonstrating that fracture is mainly brittle at room temperature. On the other hand, dimples can be detected on the fracture surface of the ECAP-processed samples (Fig. 14c-e) [56] and this strongly suggests that the ECAP processing causes a brittle to ductile transition in magnesium alloys which produces a considerable ductility improvement at room temperature [56,82]. Table 3 presents a summary of the mechanical properties of various Mg–Zn alloys that have undergone ECAP processing, which can be used for comparative analysis. The results demonstrate that diverse outcomes can be achieved by employing different processing conditions.

The impact of increasing ECAP passes on the microhardness of an Mg–1Zn–0.2Ca alloy is shown in Fig. 15. In the homogenized coarse-grained sample, the microhardness is 42.3 ± 4.8 Hv while the microhardness is raised to 49.6 ± 5.6 Hv after two ECAP passes and then to 59.5 ± 5.8, 63.1 ± 6.3 and 69.5 ± 6.7 Hv after four, six and eight passes, respectively. Naturally, with increasing strain, the average grain size decreases and the microhardness increases [73]. Similar results have been obtained by other studies [59,62,63,67,68].

Numerous investigations, however, have demonstrated that a reverse Hall-Petch effect exists, where texture has a significant impact on the strength of wrought magnesium alloys [117–119]. Room temperature tensile curves of the Mg–5.12Zn–0.32Ca alloy in the as-extruded and ECAP-processed conditions are shown in Fig. 16. Compared to the as-extruded

Table 3
Summary of the obtained average grain size and mechanical properties of different Mg–Zn alloys processed through ECAP.

Alloy & ECAP state	Average grain size (μm)	TYS (MPa)	UTS (MPa)	Elongation (%)	Ref.
ZE41A (as-cast)	~ 80	~ 130	~ 200	~ 8.5	[92]
8 P at 330 °C	~ UFG + ~70	~ 250	~ 280	~ 4	
16 P at 330 °C	UFG + 5–8	~ 270	~ 305	~ 11	
32 P at 330 °C	1.5	~ 285	~ 320	~ 14	
Mg–5.25Zn–0.6Ca (as-extruded)	3.9	178	276	25.9	[89]
4 P at 250 °C by Rout A	1.0	246	332	15.5	
4 P at 250 °C by Rout Bc	0.7	180	287	21.9	
4 P at 250 °C by Rout C	0.8	131	228	12.6	
ZE41 (as-received)	~ 50	~ 160	~ 240	~ 8	[87]
6 P at 320 °C	~ 2	~ 230	~ 325	~ 20	
ZK60 (as-solution)	~ 10 + ~ 200	-	-	-	[85]
4 P at 240 °C	~ 1.8	120	221	22.2	
8 P at 240 °C	~ 1.6	125	226	28.9	
4 P at 240 °C + 4 P at 180 °C	~ 0.8	175	266	25.9	
ZK60 (as-received)	~ 1–2 + ~ 10–20	~ 290	~ 340	~ 15	[84]
4 P at 250 °C	-	~ 230	~ 310	~ 17	
4 P at 200 °C	-	~ 216	~ 305	~ 21	
4 P at 150 °C	0.6	~ 273	~ 300	~ 32	
8 P at 150 °C	1	~ 219	~ 290	~ 25	
ZK60 (as-received)	3.8 + 37.3	~ 210	285	~ 15	[82]
1 P at 250 °C	-	~ 175	~ 290	~ 20	
2 P at 250 °C	-	~ 175	326	~ 24	
3 P at 250 °C	-	~ 170	~ 315	~ 27	
4 P at 250 °C	2.4 + 10.9	~150	~ 305	~ 30	
ZK60 (as-cast)	150	-	-	-	[76]
8 P at 300 °C	-	193	265	19	
12 P at 300 °C	-	181	289	23.6	
ZK60 (hot pressed)	70	222	264	7.4	[75]
2 P at 250 °C	~ 4.4	180	277	24	
Mg–6 Zn (as-homogenized)	-	75	290	26	[44]
Mg–12 Zn (as-homogenized)	-	150	362	19	
Mg–6 Zn (4 P at	-	302	314	0.7	
220+220+220+160 °C)	-	385	391	0.6	
Mg–12 Zn (4 P at					
200+185+170+155 °C)					
Mg–1Zn–0.2Ca (as-homogenized)	270	34	138	-	[73]
8 P at 400+350+300+250 °C	2	205	282	-	
Mg–5Zn–0.5Ca–0.3Mn (as-extruded)	4	~ 241	~ 304	~ 11.5	[68]
1 P at 250 °C	1.8	~ 182	~ 293	~ 25.6	
2 P at 250 °C	1.5	~ 227	~ 306	~ 19.2	
3 P at 250 °C	1.3	~ 235	~ 307	~ 21.9	
4 P at 250 °C	0.9	~ 252	~ 309	~ 18.5	
Mg–2Zn–2Gd–0.5Zr (as-cast)	~25	-	-	-	[63]
2 P at 380 °C	~ 3.5	~ 195	~ 230	~ 25	
4 P at 380 °C	~ 2	~ 230	~ 280	~ 33	
Mg–1.62Zn–0.55Zr-0.38Y (as-extruded)	~ 3	~ 300	~ 325	~ 17	[60]
2 P at 380 °C	-	~ 220	~ 270	~ 22	
4 P at 380 °C	~ 1.37	~ 177	~ 260	~ 27	
ZX00 (as-extruded)	~ 5.9	~ 225	~ 256	~ 21	[59]
D-ECAP: 1 P at 300 °C	~ 2.1	~ 227	~ 269	~ 17	
D-ECAP: 1 P at 280 °C	~ 1.5	~ 214	~ 265	~ 9	
D-ECAP: 2 P at 300 °C	~ 2.2	~ 284	~ 298	~ 26	
D-ECAP: 2 P at 280 °C	~ 1.3	~ 329	~ 345	~ 9	
D-ECAP: 4 P at 300 °C	~ 1.7	~ 322	~ 324	~ 11	
D-ECAP: 4 P at 280 °C	~ 1.5	~ 372	~ 375	~ 7	
ZM21 (as-rolled)	45	~ 150	~ 243	~ 20	[58]
1 P at 220 °C	18.4	~ 136	~ 228	~ 21	
2 P at 220 °C	10.9	~ 154	~ 215	~ 22	
3 P at 220 °C	5.0	~ 128	~ 212	~ 23	
4 P at 220 °C	5.4	~ 137	~ 227	~ 27	

(*continued on next page*)

Table 3 (*continued*)

Alloy & ECAP state	Average grain size (μm)	TYS (MPa)	UTS (MPa)	Elongation (%)	Ref.
Mg–4.18Zn–1.08Mn (as-homogenized)	~ 260	~ 92	~ 106	~ 5.8	[57]
1 P at 300 °C	~ 64	~ 117	~ 153	~ 7.5	
2 P at 300 °C	~ 40	~ 124	~ 193	~ 16.5	
3 P at 300 °C	~ 12	~ 174	~ 234	~ 18	
4 P at 300 °C	~ 8	~ 156	~ 218	~ 21	
ZK60 (as-homogenized)	~ 102	~ 80	~ 200	~ 13	[56]
6 P at 240 °C	~ 3.5	~ 170	~ 260	~ 28	
ZK30 (as-received)	26.69	~ 80	~ 238	~ 20.6	[54]
1 P at 250 °C	3.24	~ 92	~ 332	~ 31.6	
4 P at 250 °C by Rout Bc	1.94	~ 95.5	~ 344	~ 27	
4 P at 250 °C by Rout A	2.89	~ 93	~ 330	~ 29.7	
4 P at 250 °C by Rout C	2.25	~ 95	~ 338	~ 28.5	
Mg–1Zn-–0.2Ca (as-homogenized)	415	~ 65	~ 119	~ 9	[53]
4 P at 430+430+400+350 °C	5 + 40	~ 97	~ 210	~ 23	
ZN20 (as-extruded)	~ 10–40	~ 210	~ 240	~ 22	[50]
4 P at 300 °C	~ 10	~ 213	~ 240	~ 32	
4 P at 350 °C	-	~ 189	~ 222	~ 28	

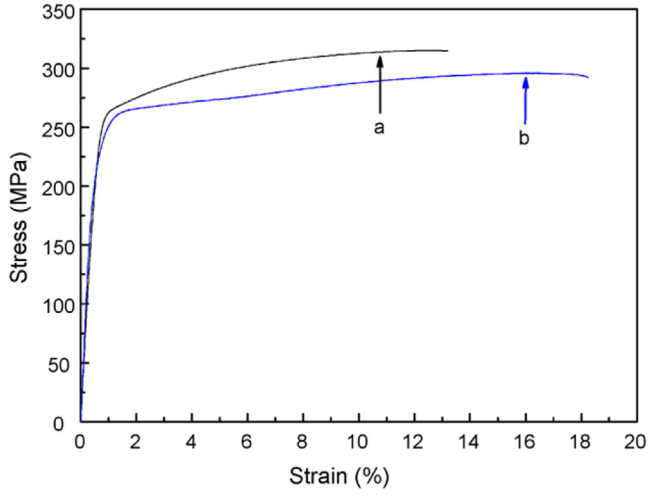

Fig. 16. Room temperature tensile curves of the Mg–5.12Zn–0.32Ca alloy in the (a) as-extruded and (b) ECAP conditions [90].

alloy, the ECAP-processed alloy with finer grains has a greater elongation to failure but a lower yield stress and ultimate tensile strength [90] by contrast to the predictions of the Hall-Petch equation. This has been reported also in other research [60,82,84]. In order to explain the observed pattern, factors other than grain size should be taken into account. The main cause of the decline is texture modification which results in an increased Schmid factor [84]. Fig. 17 depicts the distributions of Schmid factor for the basal slip system in ECAP-processed ZK60 samples derived using EBSD data. As the Schmid factor for basal slip increased with increasing numbers of ECAP passes so a lower stress was required for yielding. These results show that texture softening predominates over grain boundary strengthening [60,90].

In addition to the number of ECAP passes, other variables such as pre-treatment, temperature and processing route, which were effective for the microstructural evolution as discussed in the preceding section, also affect the mechanical behavior of the ECAP-processed magnesium-zinc alloys. In this respect, for example, it was reported [76] that a pre-solution treatment increases the ductility and strength of the ECAP-processed ZK60 alloy. Additionally, it was found that processing ECAP at a lower temperature, in the range of 150–250 °C by comparison with 350 °C, boosts the strength but decreases the ductility. In another investigation [85], it was revealed that a two-step ECAP process of 4 passes at 240 °C + 4 passes at 180 °C allowed the ZK60 alloy to be deformed by ECAP at low temperatures and thus is more effective in grain refinement than the single-step ECAP process of 8 passes at 240 °C. For this alloy, the yield strength, 175 MPa, and ultimate tensile strength, 266 MPa, of the two-step ECAP processing are higher than those of the single-step ECAP processing which are 125 MPa and 226 MPa, respectively.

Tensile curves of the Mg–5.25Zn–0.6Ca alloy in different conditions are shown in Fig. 18. It can be observed that the strength of the as-extruded alloy is improved after ECAP processing by routes *A* and *Bc* whereas route *C* shows a decreased trend, an effect which was related to the different textures developed after different processing routes [89].

Another crucial mechanical aspect that biodegradable magnesium alloys must possess is adequate fatigue life in order to prevent fracture before the patient has fully recovered. Clearly, grain size has little to no impact on the cyclic response when dislocations only move over short distances relative to the grain size. However, when the grain sizes are sufficiently small, as in the ECAP-processed alloys, the grain boundaries act as the primary barrier to dislocation motion and then the cyclic behavior will be affected by grain size [75]. As an example of this effect, it was reported [66] that the grain refinement brought on by ECAP increased the fatigue limit of an Mg–1Zn–0.3Ca alloy from 100 MPa in the initial state (homogenized + extruded + annealed) to 110 MPa after processing by ECAP for 10 passes (Fig. 19).

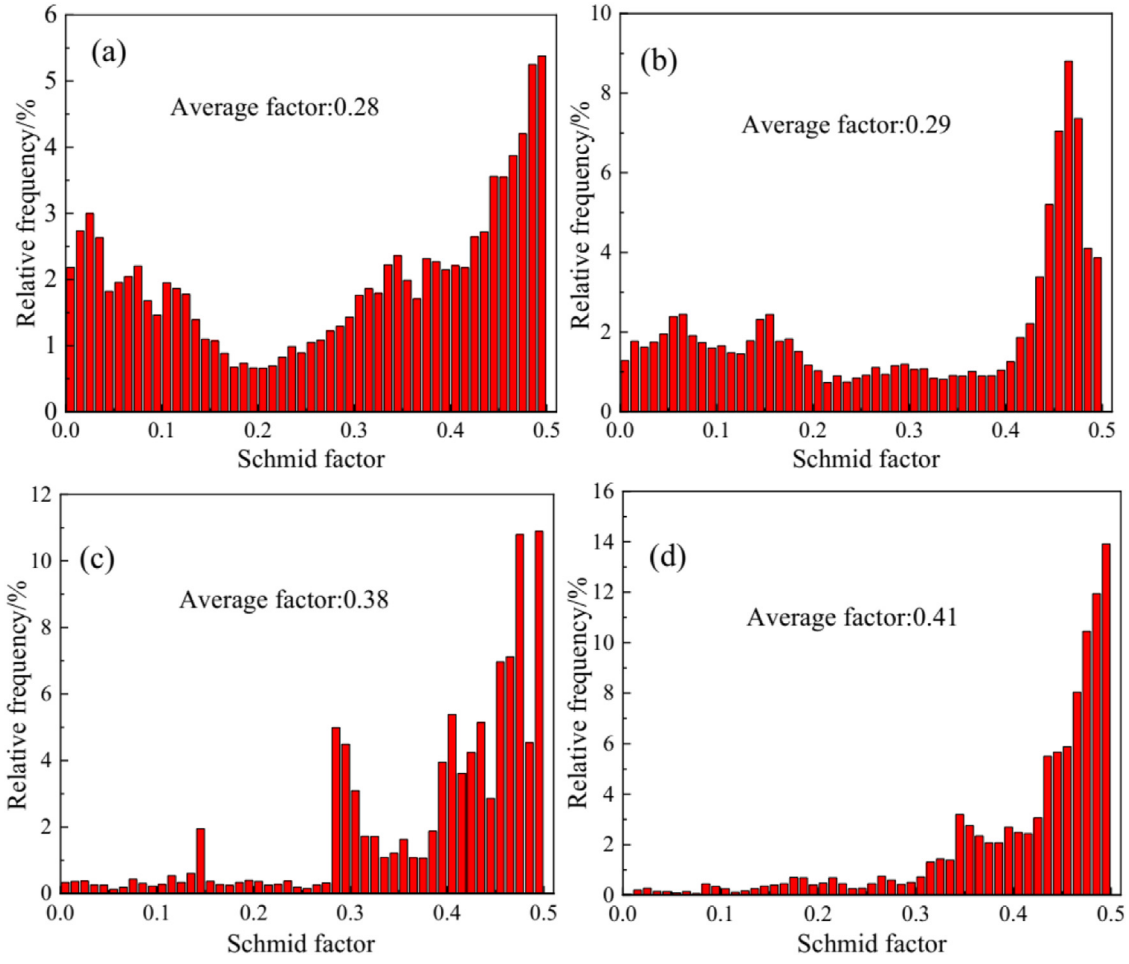

Fig. 17. Basal slip Schmid factor distribution histogram of the ECAP-processed ZK60 specimens: (a) 1 pass, (b) 2 passes, (c) 4 passes and (d) 6 passes [56].

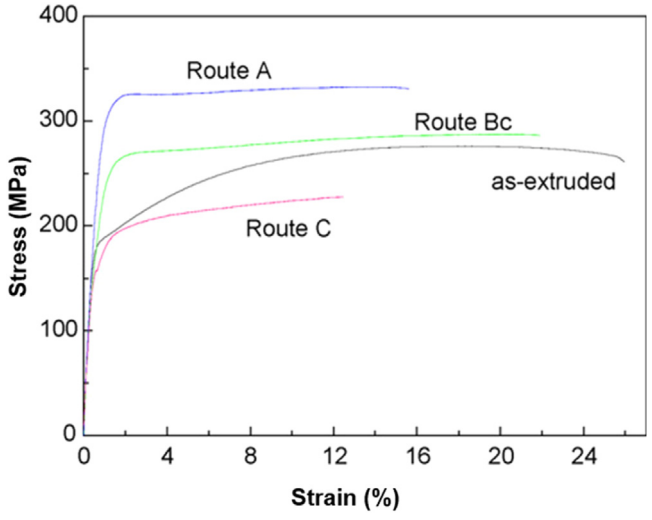

Fig. 18. Tensile curves of the Mg–5.25Zn–0.6Ca alloy in the as-extruded, ECAP-route A, ECAP route Bc and ECAP-route C conditions [89].

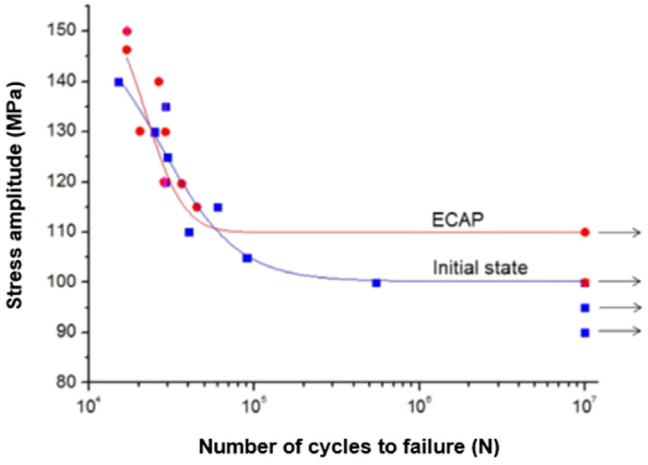

Fig. 19. Effect of ECAP (10 passes using route Bc) on fatigue behavior of the Mg–1Zn–0.3Ca alloy [66].

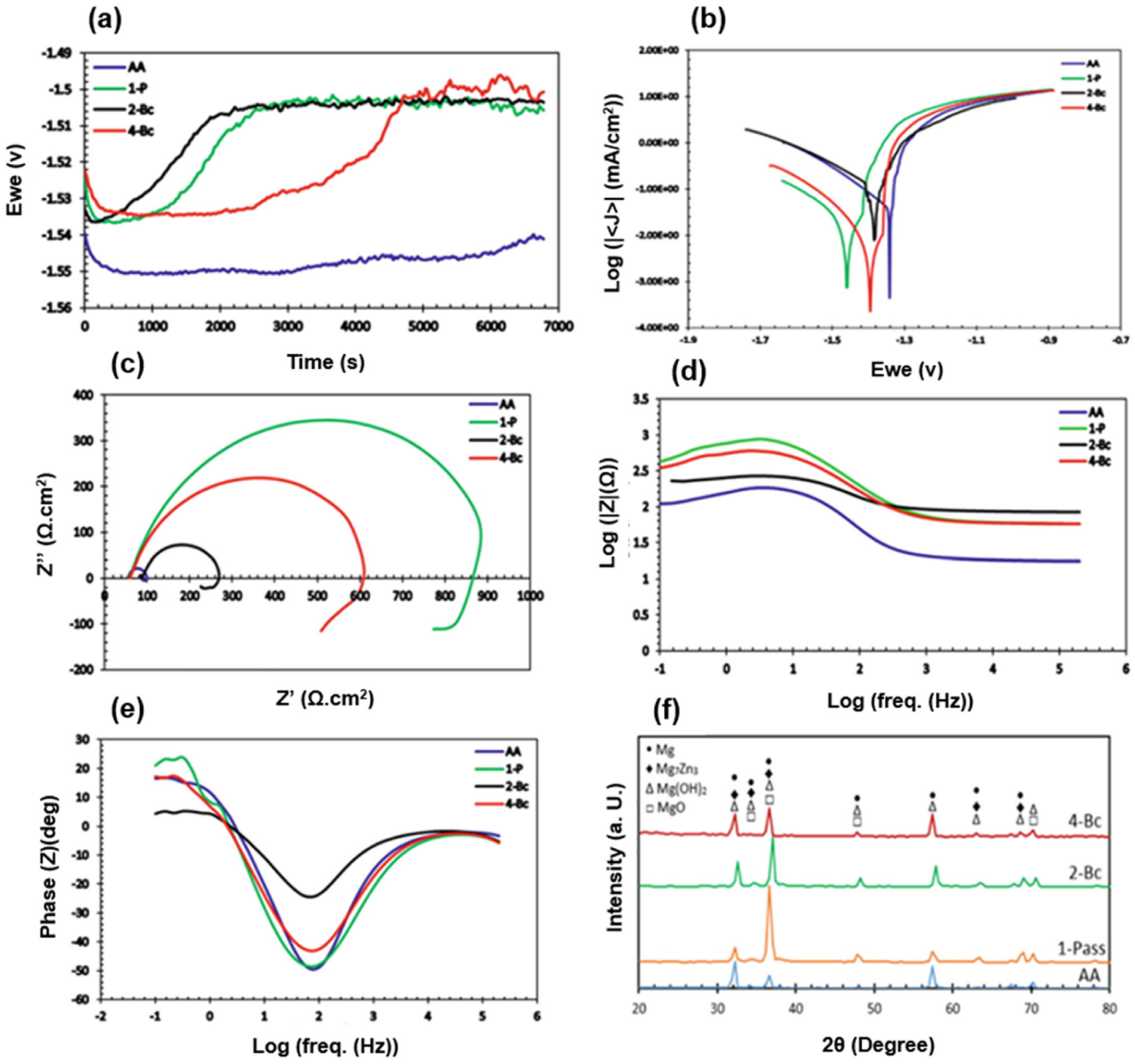

Fig. 20. OPC curves (a), potentiodynamic polarization curves (b), Nyquist plot (c), Bode plot (d), phase angle (e), and X-ray diffraction patterns (f) of the ZK30 alloy in different conditions of as-annealed (AA), 1 pass of ECAP (1-P), 2 passes of ECAP (2-P) and four passes of ECAP (4-P) [5].

3.3. Degradation behavior

Generally, the degradation behavior of magnesium alloys is dependent on several factors, including the alloy properties such as composition, background, microstructure, texture and the state of secondary phases, surface quality, and the corrosive environmental conditions such as the type of solution, temperature and retention time. Thus, ECAP processing parameters such as the number of passes, the die angle and the processing route can affect the degradation behavior of magnesium alloys.

In practice, the anodic partial reaction happens when magnesium dissolves and an electron is released, as described in Eq. (10), while at the cathode this electron is absorbed causing hydrogen to be evolved (Eq. (11)). In addition to electrochemical corrosion, a chemical reaction known as anodic hydrogen evolution causes magnesium to be dissolved (Eq. (12)). Magnesium corrosion in both the electrochemical and chemical modes is a part of the total reaction shown in Eq. (13). Eq. (14) also covers the creation of corrosion products [58]:

$$2Mg \rightarrow 2Mg^{+} + e \text{ (anodic partial reaction)} \quad (10)$$

$$2H^{+} + 2e \rightarrow H_2 \text{ (cathodic partial reaction)} \quad (11)$$

$$2Mg^{+} + 2H_2O \rightarrow 2Mg^{2+} + 2OH^{-} + H_2 \text{ (chemical reaction)} \quad (12)$$

$$2Mg + 2H^{+} + 2H_2O \rightarrow 2Mg^{2+} + 2OH^{-} + 2H_2 \text{ (overall reaction)} \quad (13)$$

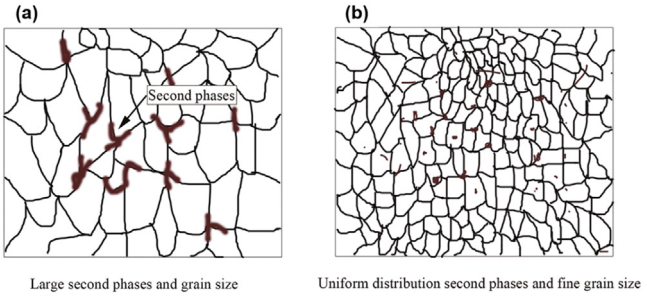

Fig. 21. Schematic illustration of the effect of ECAP on the morphology and distribution of second phase particles, and thus the corrosion resistance of Mg alloys. (a) large second phases and grain size in the as-cast alloy, (b) the grain size reduction and uniform distribution of second phases after two passes of ECAP. Reproduced from [63].

$$Mg^{2+}+2OH^{-} \rightarrow Mg(OH)_2(\text{product formation}) \quad (14)$$

It is difficult to firmly identify the effect of ECAP on the corrosion resistance of magnesium alloys [66]. While some studies indicate that ECAP processing reduces the corrosion of magnesium alloys, others suggest that it has little to no impact. However, it is well-known that the presence and morphology of second phases, grain size [120] and also texture [11] affect the corrosion resistance of the magnesium alloy.

The electrochemical behavior of a ZK30 alloy in the as-annealed (AA) and ECAP-processed states is shown in Fig. 20. As can be seen, the corrosion resistance increases after 1 pass of ECAP by comparison with the AA sample, while the resistance decreases after the second pass compared to the 1 pass, and then increases again after the fourth pass. In general, it is concluded that the corrosion resistance increases after ECAP processing. The fine-grained microstructure together with the uniform dispersion of the secondary phase particles (Mg_7Zn_3) achieved as a result of ECAP led to the production of a more protective layer ($Mg(OH)_2$). The observed decrease in the corrosion resistance after the first pass is attributed to the increase in the density of dislocations due to strain accumulation [5]. Similarly, by using several ECAP routes, comparable results were reported for a ZK30 alloy [54].

In addition to the nature of the second phase particles, their size and distribution can greatly influence the corrosion resistance of Mg alloys [121]. This seems more important considering the fact that ECAP can significantly affect these microstructural features. Fig. 21 schematically illustrates the impact of ECAP processing on the distribution of particles. Prior to extrusion, the alloy contained numerous large and coarse second phases, which negatively impacted the corrosion resistance (Fig. 21a). However, after undergoing two passes of ECAP, the second phases transformed from large to small sizes and achieved a more uniform distribution. The presence of small and uniformly distributed second phases is known to inhibit the micro-galvanic effect. Additionally, the grain size of the alloy was significantly reduced, and the grains exhibited greater uniformity compared to the as-cast alloy (Fig. 21b). As a result, the corrosion resistance of the alloy was substantially improved [63]. The surface morphology of the as-received extruded and ECAP-processed ZK60 samples after 96 h immersion in the PBS solution and after removing the corrosion products by chromic acid are shown as stereoscopic pictures in Fig. 22. As demonstrated in Fig. 22a, large pits are visible on the surface of the extruded sample, confirming the severity of the localized corrosion, mainly due to the large and non-uniformly dispersed intermetallic particles [84]. The micro-galvanic impact is thought to be more significant, fostering severe corrosion conditions near second-phase particles that are quite coarse [122,123]. On the other hand, such large pits are rarely observed on the surface of the corroded ECAP-processed sample (Fig. 22b) which is mainly due to the effect of ECAP on the morphology of the second phase particles where localized corrosion is restricted to smaller areas and a more uniform corrosion regime primarily contributes to the observation of degradation [84]. Other studies [69,93] have also discovered similar findings.

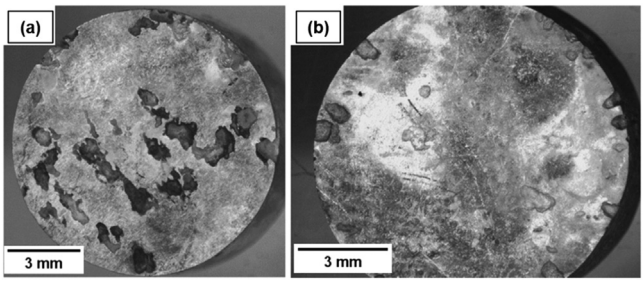

Fig. 22. General view of the corrosion surfaces of the ZK60 alloy after immersion in PBS for 96 h: (a) as-received extruded sample, and (b) ECAP-processed sample. Reproduced from [84].

A bimodal microstructure, which is easily observed in the ECAP-processed magnesium alloys, seems to have no significant beneficial effect on the corrosion resistance. It has been suggested that there may be a potential difference between large and ultra-fine grains [122]. Thus. large grains have a relatively greater potential acting as the cathode, whereas ultra-fine grains have a relatively lower potential working as the anode. This can produce a decreased corrosion resistance as a result of galvanic corrosion [60].

In addition to grain size, the texture also affects the corrosion resistance of magnesium alloys. The surface energies of the basal (0001), prismatic $\{10\bar{1}0\}$ and pyramidal $\{11\bar{2}0\}$ planes of magnesium have been reported as 1.54×10^4 J mol^{-1}, 3.04×10^4 J mol^{-1}, and 2.99×10^4 J mol^{-1}, respectively [124]. Atomic diffusion is slowed down by a lower surface energy. As a result, the corrosion resistance should decrease in the following order: basal plane, pyramidal plane and then prismatic plane [50].

Fig. 23 shows macroscopic images of immersed ZM21 alloy samples. As-cast samples consistently exhibited less corrosion than the ECAP samples, and ECAP samples exhibited higher macroscopic corrosion, particularly towards the sample corners with prolonged immersion. The sample lost its original shape in the worst situation which was in Hank's solution. On all samples, whitish insoluble salt precipitates and

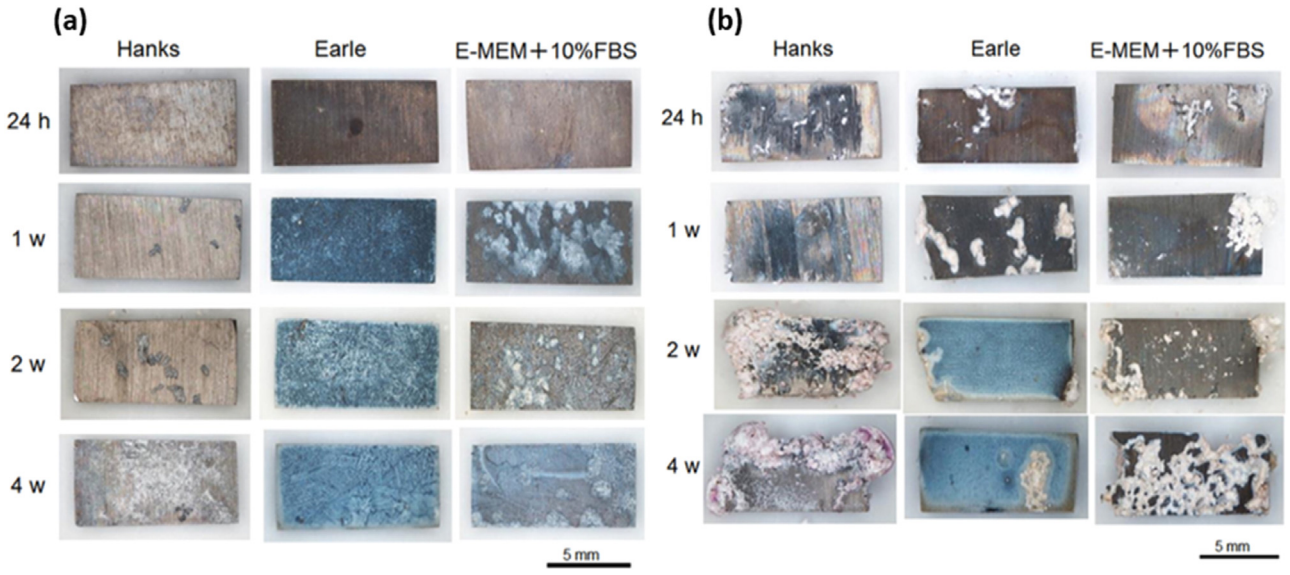

Fig. 23. Macroscopic images of as-cast (a) and ECAP-processed (b) ZM21 samples after immersion for 24 h, 1 week, 2, and 4 weeks in Hanks', Earle's, and E-MEM + 10% FBS solutions [78].

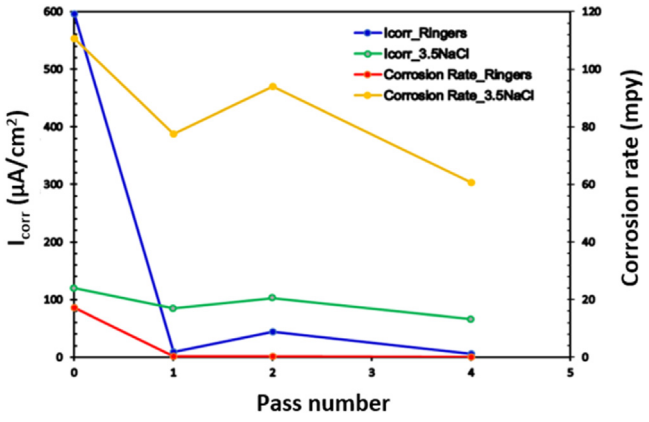

Fig. 24. Comparison between the corrosion rate and I_{corr} for ZK30 in ringer and 3.5% NaCl solution [55].

pitting corrosion signs can be seen [78]. According to the relevant research [125], the corrosion primarily occurs at surface defects such as grain boundaries and dislocations. The ECAP-processed samples have more nucleation sites and thus are better able to create an insoluble salt layer because they have a higher proportion of crystalline defects with a higher energy and reactivity. Additionally, due to their greater surface energy as a result of texture formation, the ECAP samples exhibit more localized corrosion which mostly occurs near the sample edges [78].

The effect of the number of ECAP passes on the corrosion behavior of a ZK30 alloy in the presence of two types of corrosion agents, ringer lactate and sodium chloride, was investigated [55] and the results are presented in Fig. 24 where the corrosion current density (I_{corr}) and corrosion rates of the samples are compared in both solutions. In all processing circumstances, the 3.5% NaCl solution corroded more quickly than the ringer solution. The increased concentration of chloride ions is responsible for this faster corrosion rate [55].

The use of protective coatings is a useful method for reducing the fast degradation rate of biodegradable magnesium alloys. In addition to the fact that the surface quality of the substrate is important for coating, it is also of considerable importance that the surface quality has a direct and significant impact on the corrosion of magnesium alloys, where the surface roughness has a direct effect on corrosion [126–128]. For coating applications, ECAP-processing may offer an excellent substrate. The cross-sectional micrographs and surface morphologies of hydrothermally-coated Mg–4Zn and Mg–4Zn–0.5Ca alloys are shown in Fig. 25. In Fig. 25a and b, there is a loose and a non-uniform coating formed on the extruded Mg–4Zn alloy where it is also possible to see quite large cracks. The addition of Ca to the extruded Mg–4Zn alloy produced a more uniform structure with shorter cracks and voids in the coating, as seen in Fig. 25c and d. Additionally, a cross-sectional micrograph of the ECAP-processed Mg–4Zn–0.5Ca alloy shows a compact and uniform coating with a dense structure and with nearly no discernible cracks (Fig. 25f). These results demonstrate the significant impact of the substrate on the effectiveness of hydrothermally produced coatings on magnesium alloys. Since atoms deposited at grain boundaries are at greater energy levels than other atomic sites in the lattice, smaller grains will offer more locations for the coating to precipitate. Because of this, they can provide a stronger driving force to improve the nucleation of the coating during the hydrothermal reaction. Additionally, due to the greater numbers of nucleation sites on a fine-grained substrate as opposed to a coarse-grained sample, the coating nucleation will be more uniform. The enhanced substrate corrosion resistance created by this compact, thick and defect-free coating resulted in a noticeably slower rate of degradation in a Mg–4Zn–0.5Ca alloy [20].

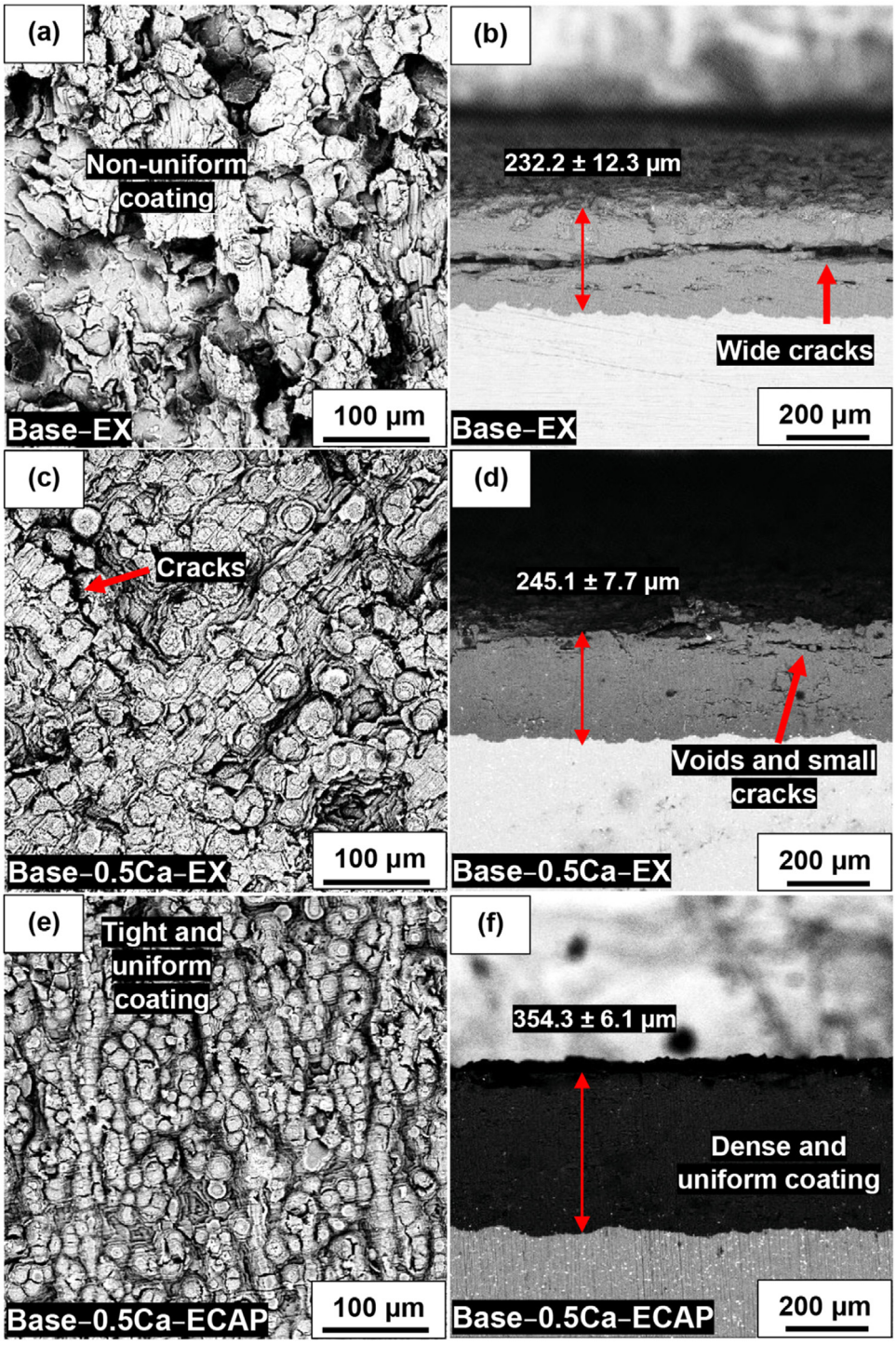

Fig. 25. SEM micrographs of surface morphology and cross-section of: (a,b) extruded Mg-4 Zn alloy, (c,d) extruded Mg–4Zn–0.5Ca alloy, and (e,f) ECAP-processed Mg–4Zn–0.5Ca alloy [20].

Similar results were also obtained in another investigation [61] by ECAP processing and applying micro-arc oxidation (MAO) composite coating on a Mg–4.71Zn–0.6Ca alloy. The weight loss percentage and corrosion surface morphology of several treated Mg–4.71Zn–0.6Ca alloys in Hank's solution during a 36-day period are shown in Fig. 26. The weight loss percentage of the as-cast sample is higher than for the ECAP-processed sample while the weight loss percentage of the MAO samples is much lower than for the Mg–4.71Zn–0.6Ca alloy samples without MAO treatment (Fig. 26a). The ECAP/MAO sample, which had a denser MAO coating and smaller micro-pores than the as-cast/MAO sample, was more

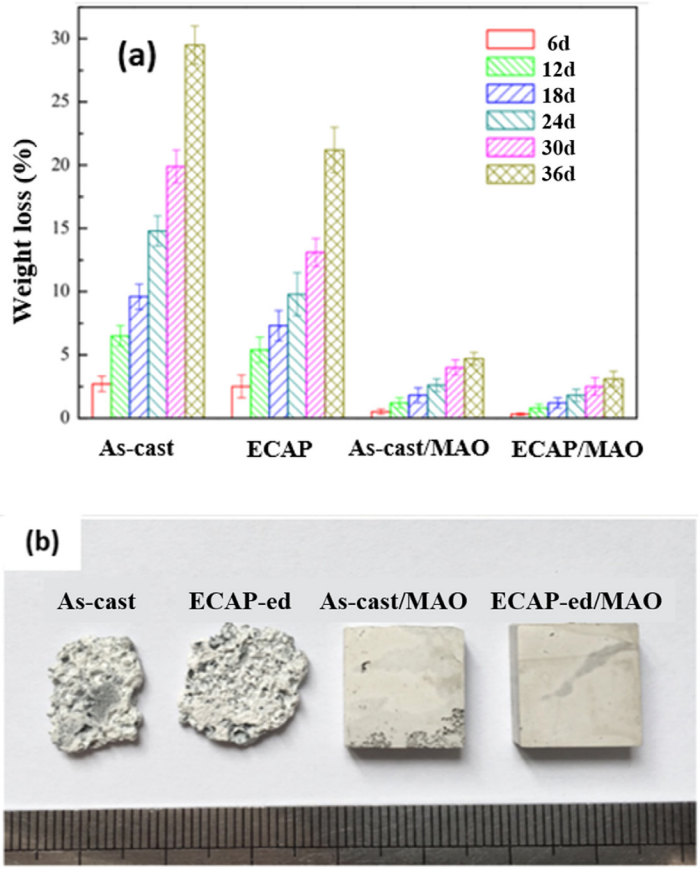

Fig. 26. (a) Weight loss results, and (b) corrosion surface morphology after 36 days of immersion in Hank's solution, for the as-cast and ECAP-processed Mg–4.71Zn–0.6Ca alloy samples, with and without MAO coating [61].

successful in preventing corrosion solution contact and penetration into the alloy substrate (Fig. 26b). Therefore, the ECAP/MAO sample has the lowest corrosion rate after being immersion in Hank's solution for 36 days and it exhibited better long-term corrosion resistance [61].

3.4. Biocompatibility and cytotoxicity

The possible effect of ECAP processing on the cytotoxicity and biocompatibility of Mg–Zn alloys has been studied to a limited extent. In this respect, Fig. 27 illustrates the cell viability and the analysis of live/dead MG63 cell labeling using fluorescent pictures for a ZM21 alloy processed by four ECAP passes. It is observed that a significant number of live cells were detected in the ECAP-processed sample compared to the untreated sample. In another study [94], the Mg–3Zn–0.2Ca alloy processed by six ECAP passes showed no significant cytotoxicity to L-929 cells. Thus, microstructural modifications due to ECAP processing can alter the biocompatibility of Mg–Zn based alloys in addition to the mechanical and degradation behavior [58].

The effect of ECAP and MIF (multiaxial isothermal forging) on the morphology and cytotoxicity of the ZK60 alloy has been studied [95]. The results obtained indicate no significant changes in the cell morphology when exposed to extracts (Fig. 28a-d). The MIF-processed ZK60 alloy, however, had a noticeably decreased cell density in cytostatic mitomycin micrographs (Fig. 28b). Additionally, when the ZK60/MIF sample extract was added to the cell culture, a substantial rise in the proportion of necrotic cells was observed (Fig. 28e). Overall, the MIF-processed ZK60 alloy showed greater toxicity than the ECAP-processed ZK60 alloy. This might be as a result of the higher rate of corrosion in this sample, which would raise the pH of the solution and alter cytotoxicity [95].

To conduct a comprehensive analysis of the effect of ECAP processing on the biocompatibility of the Mg–1.0Zn–0.3Ca alloy, in-vitro and in-vivo biocompatibility studies were performed [96]. In-vitro tests of blood cell cytotoxicity and hemolytic activity revealed no statistically significant differences between the two outcomes before and after ECAP (Fig. 29a). Following the determination of the alloy's biocompatibility, particular alloy characteristics were assessed. It should be noted that osteoconduction (the capacity to promote the adhesion of osteogenic cells) and osteoinduction (the capacity to induce the differentiation of multipotent cells into osteogenic cells) are crucial properties to take into ac-

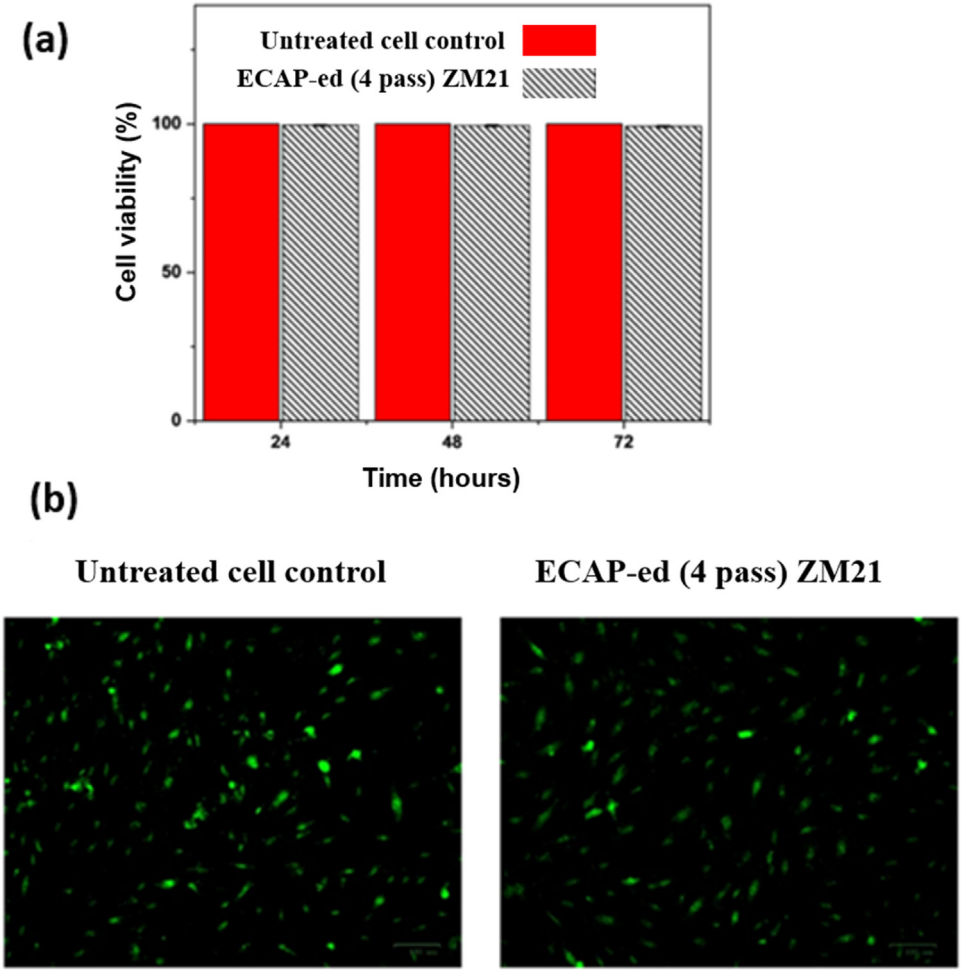

Fig. 27. (a) Cell viability as a function of time, and (b) live/dead staining of MG63 cells on untreated (left) and ECAP treated for four passes (right) ZM21 alloy. Reproduced from [58].

count when determining whether an implant material is suitable for successful osteoreconstruction. Both forms of the alloy demonstrated osteoconductive activity by promoting cell adhesion, as shown in Fig. 29b. However, compared to the control group, cell proliferation was reduced after multipotent mesenchymal stromal cells (MMSCs) were incubated on the surface of the alloy for an extended period of time. The membrane protein alkaline phosphatase (ALP), a marker of osteoblasts, was induced by the addition of extracts of both types of the alloy to the incubation medium. Compared to the homogenized alloy, the activity of the alloy was slightly more obvious following ECAP. Mice were implanted with alloy samples to examine the alloy's in-vivo biocompatibility. The acquired data revealed no indications of inflammation or implant rejection. However, two days following the procedure, animals with implanted alloys showed substantial edema in the implantation location due to subcutaneous gas accumulation. There were no signs of local hyperthermia, suppuration, or ulceration (Fig. 29c and d). These results support the alloy biocompatibility and safety and suggest that they are suitable as implant materials for efficient osteoreconstruction [96].

4. Perspectives and future directions

This study provides a detailed review of the effects of ECAP processing on the properties of biodegradable Mg–Zn based alloys. Processing by ECAP, by changing the microstructure including grain size, particle morphology and particle distribution and the texture, can be used to successfully improve the mechanical properties, degradation behavior and even the biological performance of Mg–Zn alloys. However, there remain numerous gaps in the available information that are now proposed for future studies:

a) Few works have been conducted on the corrosion behavior of ECAP-processed Mg–Zn based alloys in order to precisely investigate the corrosion mechanisms under various circumstances.
b) Although the mechanical properties of ECAP-processed Mg–Zn alloys have been widely studied, the fatigue properties have received only limited attention. More specifically, combinations of cyclic stresses and the corrosive nature of the human body for Mg alloys sug-

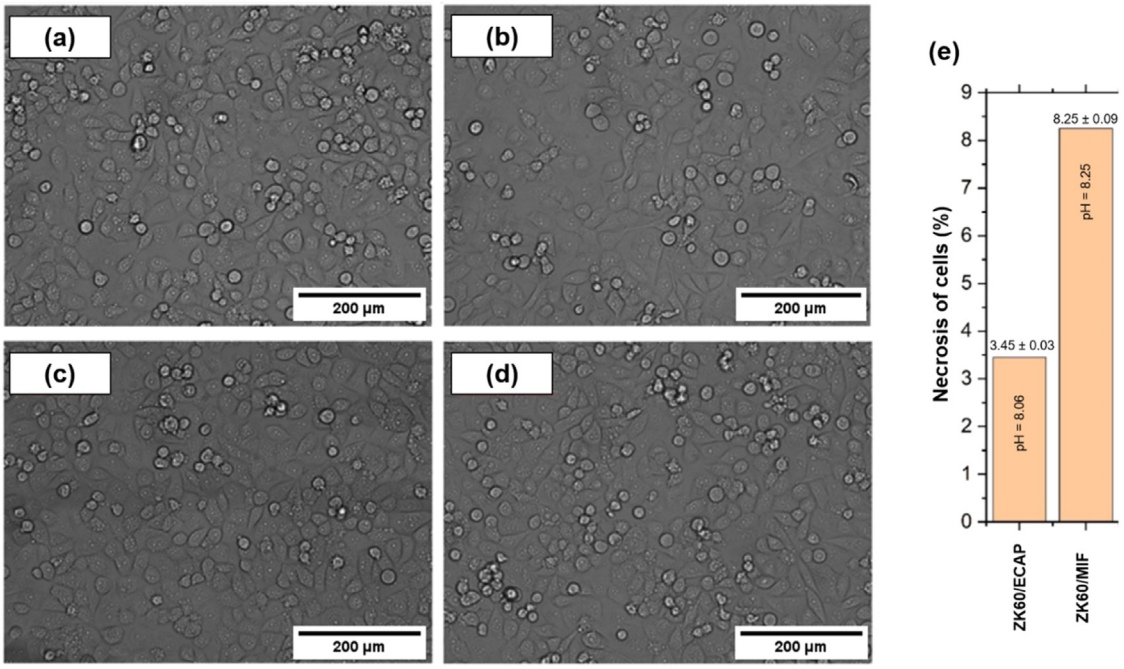

Fig. 28. Optical morphologies of the CRL-4058 cells after 24 h incubation with extracts of: (a) ECAP-processed ZK60 alloy, and (b) MIF-processed ZK60 alloy. (c) The positive control (cytostatic mitomycin), and (d) the negative control (cells with culture medium). (e) The percentage of necrotic cells in the population of immortalized human fibroblasts after incubation with extracts (iodide propidium staining, analysis of at least 60,000 cells). Reproduced from [95].

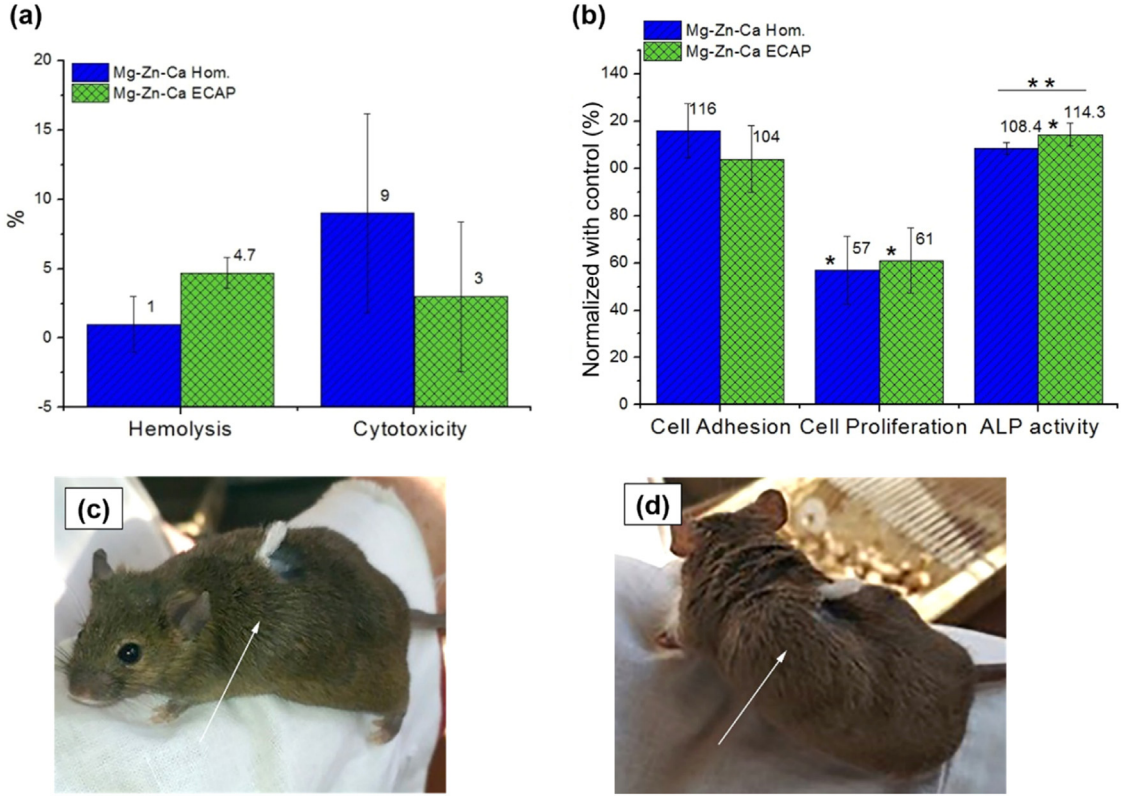

Fig. 29. Comparison of the in-vitro biocompatibility (a) and Osteoconduction and osteoinduction (b) of the Mg–1.0Zn–0.3Ca alloy in the homogenized and ECAP-processed conditions. Accumulation of gas at the implantation site, two days after surgery, for the homogenized (c) and ECAP-processed (d) alloy. Reproduced from [96].

gest that corrosion-fatigue is of great importance for biodegradable magnesium alloys.

c) As already noted, ECAP processing has little or no impact on the biocompatibility and cytotoxicity of biodegradable Mg alloys. However, to precisely establish the scope of these effects, more research is needed including both in-vitro and in-vivo experiments.

Declaration of competing interest

The authors declare that they have no known competing financial interests or personal relationships that could have appeared to influence the work reported in this paper.

Acknowledgement

The work of one of the authors was supported by the European Research Council under Grant Agreement No. 267464-SPDMETALS (TGL).

References

[1] F. Witte, I. Abeln, E. Switzer, V. Kaese, A. Meyer-Lindenberg, H. Windhagen, J. Biomed. Mater. Res. Part A 86A (2008) 1041–1047.
[2] M.P. Staiger, A.M. Pietak, J. Huadmai, G. Dias, Biomaterials 27 (2006) 1728–1734.
[3] R. Radha, D. Sreekanth, J. Magnes. Alloy. 5 (2017) 286–312.
[4] Y.F. Zheng, X.N. Gu, F. Witte, Mater. Sci. Eng. R Rep. 77 (2014) 1–34.
[5] W.H. El-Garaihy, A.I. Alateyah, M.O. Alawad, T.A. Aljohani, in: 2022, pp. 259–269.
[6] K. Bryła, J. Horky, M. Krystian, L. Lityńska-Dobrzyńska, B. Mingler, Mater. Sci. Eng. C 109 (2020) 110543.
[7] A.I. Alateyah, T.A. Aljohani, M.O. Alawad, H.A. El-Hafez, A.N. Almutairi, E.S. Alharbi, R. Alhamada, B.W. El-Garaihy, W.H. El-Garaihy, Metals 11 (2021) 363.
[8] A.I. Alateyah, T.A. Aljohani, M.O. Alawad, S. Elkatatny, W.H. El–Garaihy, Metals 11 (2021) 953.
[9] X. Zhang, G. Yuan, Z. Wang, Mater. Lett. 74 (2012) 128–131.
[10] M. Mohammadi Zerankeshi, R. Alizadeh, E. Gerashi, M. Asadollahi, T.G. Langdon, J. Magnes. Alloy. 10 (2022) 1737–1785.
[11] E. Gerashi, R. Alizadeh, T.G. Langdon, J. Magnes. Alloy. 10 (2022) 313–325.
[12] N. Zirak, A. Bolandparvaz Jahromi, E. Salahinejad, Ceram. Int. 46 (2020) 508–512.
[13] D.R. Lopes, C.L.P. Silva, R.B. Soares, P.H.R. Pereira, A.C. Oliveira, R.B. Figueiredo, T.G. Langdon, V.F.C. Lins, Adv. Eng. Mater. 21 (2019) 1900391.
[14] Z. Wang, N. Li, R. Li, Y. Li, L. Ruan, Prog. Nat. Sci. Mater. Int. 24 (2014) 423–432.
[15] A. Yamashita, Z. Horita, T.G. Langdon, Mater. Sci. Eng. A 300 (2001) 142–147.
[16] T.S.N. Sankara Narayanan, I.S. Park, M.H. Lee, Prog. Mater. Sci. 60 (2014) 1–71.
[17] X.-N. Gu, Y.-F. Zheng, Front. Mater. Sci. China 4 (2010) 111–115.
[18] Y. Ding, C. Wen, P. Hodgson, Y. Li, J. Mater. Chem. B 2 (2014) 1912–1933.
[19] E. Gerashi, M. Jamalpour, R. Alizadeh, S. Labbaf, R. Mahmudi, Mater. Lett. 330 (2023) 133224.
[20] M. Zohrevand, M. Mohammadi-Zerankeshi, F. Nobakht-Farin, R. Alizadeh, R. Mahmudi, J. Mater. Res. Technol. 20 (2022) 1204–1215.
[21] M. Kasaeian-Naeini, M. Sedighi, R. Hashemi, J. Magnes. Alloy. 10 (2022) 938–955.
[22] X. Li, K. Lu, Nat. Mater. 16 (2017) 700–701.
[23] R. Jahadi, M. Sedighi, H. Jahed, Mater. Sci. Eng. A 593 (2014) 178–184.
[24] R.Z. Valiev, T.G. Langdon, Prog. Mater. Sci. 51 (2006) 881–981.
[25] Z. Horita, T. Fujinami, T.G. Langdon, Mater. Sci. Eng. A 318 (2001) 34–41.
[26] R.Z. Valiev, Y. Estrin, Z. Horita, T.G. Langdon, M.J. Zechetbauer, Y.T. Zhu, JOM 58 (2006) 33–39.
[27] A.P. Zhilyaev, T.G. Langdon, Prog. Mater. Sci. 53 (2008) 893–979.
[28] M.A. Salevati, F. Akbaripanah, R. Mahmudi, K.H. Fekete, A. Heczel, J. Gubicza, Mater. Sci. Eng. A 776 (2020) 139002.
[29] E. Gerashi, R. Alizadeh, R. Mahmudi, J. Mater. Res. Technol. 20 (2022) 3363–3380.
[30] C. Cui, J. He, W. Wang, W. Chen, W. Zhang, J. Alloys Compd. 909 (2022) 164795.
[31] Q. Wang, Y. Chen, M. Liu, J. Lin, H.J. Roven, Mater. Sci. Eng. A 527 (2010) 2265–2273.
[32] H. Wang, W. Chen, W. Zhang, D. Fang, S. Wang, W. Wang, Mater. Sci. Eng. A 806 (2021) 140807.
[33] M. Ebrahimi, Q. Wang, S. Attarilar, Prog. Mater. Sci. 131 (2023) 101016.
[34] Q.F. Wang, X.P. Xiao, J. Hu, W.W. Xu, X.Q. Zhao, S.J. Zhao, J. Iron Steel Res. Int. 14 (2007) 167–172.
[35] X. Rao, Y. Wu, X. Pei, Y. Jing, L. Luo, Y. Liu, J. Lu, Mater. Sci. Eng. A 754 (2019) 112–120.
[36] M. Zhan, W. Zhang, D. Zhang, Trans. Nonferrous Met. Soc. China 21 (2011) 991–997.
[37] H. Liu, J. Gan, C. Jiang, W. Wu, M. Guagliano, Surf. Coatings Technol. 441 (2022) 128601.
[38] S. Bagherifard, D.J. Hickey, S. Fintová, F. Pastorek, I. Fernandez–Pariente, M. Bandini, T.J. Webster, M. Guagliano, Acta Biomater. 66 (2018) 93–108.
[39] Z. Trojanová, Z. Drozd, K. Halmešová, J. Džugan, T. Škraban, P. Minárik, G. Németh, P. Lukáč, Materials 14 (2020) 157.
[40] Z. Trojanová, Z. Drozd, T. Škraban, P. Minárik, J. Džugan, K. Halmešová, G. Németh, P. Lukáč, F. Chmelík, Adv. Eng. Mater. 22 (2020) 1900596.
[41] G. Faraji, A. Babaei, M.M. Mashhadi, K. Abrinia, Mater. Lett. 77 (2012) 82–85.
[42] X. Li, J. Jiang, Y. Zhao, A. Ma, D. Wen, Y. Zhu, Trans. Nonferrous Met. Soc. China 25 (2015) 3909–3920.
[43] P. Minárik, E. Jablonská, R. Král, J. Lipov, T. Ruml, C. Blawert, B. Hadzima, F. Chmelík, Mater. Sci. Eng. C 73 (2017) 736–742.
[44] M. Němec, A. Jäger, K. Tesař, V. Gärtnerová, Mater. Charact. 134 (2017) 69–75.
[45] A.I. Alateyah, M.M.Z. Ahmed, M.O. Alawad, S. Elkatatny, Y. Zedan, A. Nassef, W.H. El-Garaihy, J. Mater. Res. Technol. 17 (2022) 1491–1511.
[46] A. Bahmani, M. Lotfpour, M. Taghizadeh, W.-J. Kim, J. Magnes. Alloy. 10 (2022) 2607–2648.
[47] S. Zhang, X. Zhang, C. Zhao, J. Li, Y. Song, C. Xie, H. Tao, Y. Zhang, Y. He, Y. Jiang, Acta Biomater. 6 (2010) 626–640.
[48] S. Cai, T. Lei, N. Li, F. Feng, Mater. Sci. Eng. C 32 (2012) 2570–2577.
[49] J. Kubásek, D. Vojtěch, J. Mater. Sci. Mater. Med. 24 (2013) 1615–1626.
[50] M. Gao, K. Yang, L. Tan, Z. Ma, J. Magnes. Alloy. 10 (2022) 2147–2157.
[51] M. Gao, I.P. Etim, K. Yang, L. Tan, Z. Ma, Mater. Sci. Eng. A 829 (2022) 142058.
[52] M.O. Alawad, A.I. Alateyah, W.H. El-Garaihy, A. BaQais, S. Elkatatny, H. Kouta, M. Kamel, S. El-Sanabary, Materials 15 (2022) 7719.
[53] G. Klevtsov, R. Valiev, N. Klevtsova, M. Fesenyuk, O. Kulaysova, I. Pigaleva, Lett. Mater. 12 (2022) 203–208.
[54] A.I. Alateyah, M.O. Alawad, T.A. Aljohani, W.H. El-Garaihy, Materials 15 (2022) 6088.
[55] A.I. Alateyah, M.O. Alawad, T.A. Aljohani, W.H. El-Garaihy, Materials 15 (2022) 5515.

[56] L. Zhang, Y. Li, C. Yu, Z. Pi, Q. Shao, J. Phys. Conf. Ser. 1798 (2021) 012023.
[57] S. Ramesh, G. Kumar, C. Jagadeesh, G. Anne, H.S. Nayaka, J. Bio-Tribo-Corros. 7 (2021) 69.
[58] S. Prithivirajan, M.B. Nyahale, G.M. Naik, S. Narendranath, A. Prabhu, P.D. Rekha, J. Mater. Sci. Mater. Med. 32 (2021) 65.
[59] J. Horky, K. Bryła, M. Krystian, G. Mozdzen, B. Mingler, L. Sajti, Mater. Sci. Eng. A 826 (2021) 142002.
[60] Y. Shen, J. Chen, G. Wang, D. Cao, L. Tan, R.D.K. Misra, K. Yang, Mater. Technol. 37 (2020) 135–142.
[61] X. Ly, S. Yang, T. Nguyen, Surf. Coatings Technol. 395 (2020) 125923.
[62] S. Ramesh, G. Anne, G. Kumar, C. Jagadeesh, H.S. Nayaka, Silicon 13 (2021) 1549–1560.
[63] J.-X. Chen, X.-Y. Zhu, L.-L. Tan, K. Yang, X.-P. Su, Acta Metall. Sin. 34 (2020) 205–216.
[64] P. Sekar, N. Sanna, V. Desai, Mater. Corros. 71 (2020) 571–584.
[65] O.B. Kulyasova, I.A. Evdokimova, R.K. Islamgaliev, IOP Conf. Ser. Mater. Sci. Eng. 672 (2019) 012035.
[66] N. Martynenko, E. Lukyanova, V. Serebryany, D. Prosvirnin, V. Terentiev, G. Raab, S. Dobatkin, Y. Estrin, Mater. Lett. 238 (2019) 218–221.
[67] M. Shaeri, K. Karimi Taheri, A. Karimi Taheri, M.H. Shaeri, J. Mater. Eng. Perform. 28 (2019) 5207–5219.
[68] L.B. Tong, J.H. Chu, Z.H. Jiang, S. Kamado, M.Y. Zheng, J. Alloys Compd. 785 (2019) 410–421.
[69] K. Yan, H. Liu, N. Feng, J. Bai, H. Cheng, J. Liu, F. Huang, J. Magnes. Alloy. 7 (2019) 305–314.
[70] K. Yan, J. Sun, J. Bai, H. Liu, X. Huang, Z. Jin, Y. Wu, Mater. Sci. Eng. A 739 (2019) 513–518.
[71] K.N. Li, Y.B. Zhang, Q. Zeng, G.H. Huang, B. Ji, D.D. Yin, Mater. Sci. Eng. A 751 (2019) 283–291.
[72] D. Song, C. Li, N. Liang, F. Yang, J. Jiang, J. Sun, G. Wu, A. Ma, X. Ma, Mater. Des. 166 (2019) 107621.
[73] O.B. Kulyasova, R.K. Islamgaliev, IOP Conf. Ser. Mater. Sci. Eng. 380 (2018) 012013.
[74] M.W. Vaughan, J.M. Seitz, R. Eifler, H.J. Maier, I. Karaman, in: 2017, pp. 43–51.
[75] A. Vinogradov, J. Mater. Res. 32 (2017) 4362–4374.
[76] Y. Yuan, A. Ma, X. Gou, J. Jiang, G. Arhin, D. Song, H. Liu, Mater. Sci. Eng. A 677 (2016) 125–132.
[77] F.D. Dumitru, G. Deák, O.F. Higuera-Cobos, J.M. Cabrera-Marrero, MRS Proc. 1818 (2016) imrc2015s4g-p004.
[78] A. Witecka, A. Bogucka, A. Yamamoto, K. Máthis, T. Krajňák, J. Jaroszewicz, W. Święszkowski, Mater. Sci. Eng. C 65 (2016) 59–69.
[79] Y. Yu, S. Kuang, D. Chu, H. Zhou, J. Li, C. Li, Metallogr. Microstruct. Anal. 4 (2015) 518–524.
[80] E. Mostaed, A. Fabrizi, D. Dellasega, F. Bonollo, M. Vedani, J. Alloys Compd. 638 (2015) 267–276.
[81] D.L. Yin, H.L. Cui, J. Qiao, J.F. Zhang, Mater. Res. Innov. 19 (2015) S9-28-S9-31.
[82] F.-D. Dumitru, O.F. Higuera-Cobos, J.M. Cabrera, Mater. Sci. Eng. A 594 (2014) 32–39.
[83] E. Mostaed, M. Vedani, M. Hashempour, M. Bestetti, Biomatter 4 (2014) e28283.
[84] E. Mostaed, M. Hashempour, A. Fabrizi, D. Dellasega, M. Bestetti, F. Bonollo, M. Vedani, J. Mech. Behav. Biomed. Mater. 37 (2014) 307–322.
[85] Y. He, Q. Pan, Y. Qin, X. Liu, W. Li, J. Mater. Sci. 45 (2010) 1655–1662.
[86] R.B. Figueiredo, I.J. Beyerlein, A.P. Zhilyaev, T.G. Langdon, Mater. Sci. Eng. A 527 (2010) 1709–1718.
[87] R. Ding, C. Chung, Y. Chiu, P. Lyon, Mater. Sci. Eng. A 527 (2010) 3777–3784.
[88] L. Balogh, R.B. Figueiredo, T. Ungár, T.G. Langdon, Mater. Sci. Eng. A 528 (2010) 533–538.
[89] L.B. Tong, M.Y. Zheng, X.S. Hu, K. Wu, S.W. Xu, S. Kamado, Y. Kojima, Mater. Sci. Eng. A 527 (2010) 4250–4256.
[90] L.B. Tong, M.Y. Zheng, H. Chang, X.S. Hu, K. Wu, S.W. Xu, S. Kamado, Y. Kojima, Mater. Sci. Eng. A 523 (2009) 289–294.
[91] B. Li, S. Joshi, K. Azevedo, E. Ma, K.T. Ramesh, R.B. Figueiredo, T.G. Langdon, Mater. Sci. Eng. A 517 (2009) 24–29.
[92] A. Ma, J. Jiang, N. Saito, I. Shigematsu, Y. Yuan, D. Yang, Y. Nishida, Mater. Sci. Eng. A 513–514 (2009) 122–127.
[93] J. Jiang, A. Ma, N. Saito, Z. Shen, D. Song, F. Lu, Y. Nishida, D. Yang, P. Lin, J. Rare Earths 27 (2009) 848–852.
[94] X. Sun, Y. Su, Y. Huang, M. Chen, D. Liu, Metals 12 (2022) 685.
[95] D. Merson, A. Brilevsky, P. Myagkikh, A. Tarkova, A. Prokhorikhin, E. Kretov, T. Frolova, A. Vinogradov, Materials 13 (2020) 544.
[96] N.S. Martynenko, N.Y. Anisimova, O.V. Rybalchenko, M.V. Kiselevskiy, G. Rybalchenko, B. Straumal, D. Temralieva, A.T. Mansharipova, A.O. Kabiyeva, M.T. Gabdullin, S. Dobatkin, Y. Estrin, Crystals 11 (2021) 1381.
[97] C. Xu, K. Xia, T.G. Langdon, Mater. Sci. Eng. A 527 (2009) 205–211.
[98] Y. Iwahashi, J. Wang, Z. Horita, M. Nemoto, T.G. Langdon, Scr. Mater. 35 (1996) 143–146.
[99] M. Furukawa, Y. Iwahashi, Z. Horita, M. Nemoto, T.G. Langdon, Mater. Sci. Eng. A 257 (1998) 328–332.
[100] M. Furukawa, Z. Horita, M. Nemoto, T.G. Langdon, J. Mater. Sci. 36 (2001) 2835–2843.
[101] D. Kuhlmann-Wilsdorf, Scr. Mater. 34 (1996) 641–650.
[102] Y. He, Q. Pan, Y. Qin, X. Liu, W. Li, Y. Chiu, J.J.J. Chen, J. Alloys Compd. 492 (2010) 605–610.
[103] S.C. Baik, Y. Estrin, H.S. Kim, R.J. Hellmig, Mater. Sci. Eng. A 351 (2003) 86–97.
[104] J.D. Robson, D.T. Henry, B. Davis, Acta Mater. 57 (2009) 2739–2747.
[105] S.-J. Huang, C. Chiu, T.-Y. Chou, E. Rabkin, Int. J. Hydrogen Energy 43 (2018) 4371–4380.
[106] T. Krajňák, P. Minárik, J. Stráská, J. Gubicza, K. Máthis, M. Janeček, J. Alloys Compd. 705 (2017) 273–282.
[107] P. Minárik, R. Král, J. Čížek, F. Chmelík, Acta Mater. 107 (2016) 83–95.
[108] I.J. Beyerlein, L.S. Tóth, Prog. Mater. Sci. 54 (2009) 427–510.
[109] C. Li, H. Sun, X. Li, J. Zhang, W. Fang, Z. Tan, J. Alloys Compd. 652 (2015) 122–131.
[110] G. Timár, M.R. Barnett, J.Q. da Fonseca, Comput. Mater. Sci. 132 (2017) 81–91.
[111] M.H. Yoo, Metall. Trans. A 12 (1981) 409–418.
[112] H. Asada, H. Yoshinaga, J. Japan Inst. Met. 23 (1959) 67–71.
[113] M.R. Barnett, M.D. Nave, C.J. Bettles, Mater. Sci. Eng. A 386 (2004) 205–211.
[114] N.J. Petch, J. Iron Steel Inst. 174 (1953) 25–28.
[115] J. Koike, Metall. Mater. Trans. A 36 (2005) 1689–1696.
[116] R.B. Figueiredo, M. Kawasaki, T.G. Langdon, Prog. Mater. Sci. 137 (2023) 101131.
[117] Q. Yang, A.K. Ghosh, Acta Mater. 54 (2006) 5159–5170.
[118] Y. Wang, H. Choo, Acta Mater. 81 (2014) 83–97.
[119] H. Yu, Y. Xin, M. Wang, Q. Liu, J. Mater. Sci. Technol. 34 (2018) 248–256.
[120] Y. Lu, A.R. Bradshaw, Y.L. Chiu, I.P. Jones, Mater. Sci. Eng. C 48 (2015) 480–486.
[121] G. Song, A. Atrens, M. Dargusch, Corros. Sci. 41 (1998) 249–273.
[122] R. Zeng, K.U. Kainer, C. Blawert, W. Dietzel, J. Alloys Compd. 509 (2011) 4462–4469.
[123] A. Atrens, M. Liu, N.I.Zainal Abidin, Mater. Sci. Eng. B 176 (2011) 1609–1636.
[124] G.-L. Song, R. Mishra, Z. Xu, Electrochem. Commun. 12 (2010) 1009–1012.
[125] K.T. Aust, U. Erb, G. Palumbo, Mater. Sci. Eng. A 176 (1994) 329–334.
[126] R. Walter, M.B. Kannan, Y. He, A. Sandham, Appl. Surf. Sci. 279 (2013) 343–348.
[127] R. Walter, M.B. Kannan, Mater. Des. 32 (2011) 2350–2354.
[128] M. Gawlik, B. Wiese, V. Desharnais, T. Ebel, R. Willumeit-Römer, Materials 11 (2018) 2561.